

## The ALFA Roman Pot detectors of ATLAS

This content has been downloaded from IOPscience. Please scroll down to see the full text.

2016 JINST 11 P11013

(<http://iopscience.iop.org/1748-0221/11/11/P11013>)

View [the table of contents for this issue](#), or go to the [journal homepage](#) for more

Download details:

IP Address: 141.34.3.11

This content was downloaded on 02/01/2017 at 11:49

Please note that [terms and conditions apply](#).

You may also be interested in:

[Solid state nuclear track detectors](#)

D Henshaw

[Neutrino Masses at the LHC](#)

Frank F Deppisch

[The electronics system of the ALFA forward detector for luminosity measurements in ATLAS](#)

B Allongue, J Alozy, F Anghinolfi et al.

[Measurement of proton-proton elastic scattering and total cross-section at](#)

The TOTEM Collaboration, G. Antchev, P. Aspell et al.

[A Method to Protect CR-39 Track Detector from Sunlight](#)

N. Ahmad, Nasir M. Mirza, Sikander M. Mirza et al.

[Single track coincidence measurements of fluorescent and plastic nuclear track detectors in therapeutic carbon beams](#)

J -M Osinga, I Ambrožová, K Pachnerová Brabcová et al.

[Digital Image Analysis of Etch Pit Formation in CR-39 Track Detector](#)

Fuminobu Sato, Takahiro Kuchimaru, Yushi Kato et al.

[Engineering for the ATLAS SemiConductor Tracker \(SCT\) End-cap](#)

A Abdesselam, P P Allport, B Anderson et al.

## The ALFA Roman Pot detectors of ATLAS

S. Abdel Khalek,<sup>a</sup> B. Allongue,<sup>f</sup> F. Anghinolfi,<sup>f</sup> P. Barrillon,<sup>a</sup> G. Blanchot,<sup>f</sup> S. Blin-Bondil,<sup>a</sup> A. Braem,<sup>f</sup> L. Chytka,<sup>b</sup> P. Conde Muno,<sup>c,d</sup> M. Dren,<sup>j</sup> P. Fassnacht,<sup>f</sup> S. Franz,<sup>f</sup> L. Gurriana,<sup>c</sup> P. Grafstrm,<sup>f</sup> M. Heller,<sup>f</sup> M. Haguenaue,<sup>f</sup> W. Hain,<sup>g</sup> P. Hamal,<sup>b</sup> K. Hiller,<sup>g,1</sup> W. Iwanski,<sup>i</sup> S. Jakobsen,<sup>h</sup> C. Joram,<sup>f</sup> U. Ktz,<sup>g</sup> K. Korcyl,<sup>i</sup> K. Kreutzfeldt,<sup>j</sup> T. Lohse,<sup>l</sup> A. Maio,<sup>c,d</sup> M.J.P. Maneira,<sup>c,e</sup> A. Mapelli,<sup>f</sup> D. Notz,<sup>g,2</sup> L. Nozka,<sup>b</sup> A. Palma,<sup>c,d</sup> D. Petschull,<sup>g</sup> X. Pons,<sup>f</sup> P. Puzo,<sup>a</sup> S. Ravat,<sup>f</sup> T. Schneider,<sup>f</sup> L. Seabra,<sup>c</sup> T. Sykora,<sup>k</sup> R. Staszewski,<sup>i</sup> H. Stenzel,<sup>j</sup> M. Trzebinski,<sup>i</sup> S. Valkar,<sup>k</sup> M. Viti,<sup>g</sup> V. Vorobel<sup>k</sup> and A. Wemans<sup>c,e</sup>

<sup>a</sup>LAL, Univ. Paris-Sud, CNRS/IN2P3, Universit Paris-Saclay, Orsay, France

<sup>b</sup>Palack University, RCPTM, Olomouc, Czech Republic

<sup>c</sup>Laboratrio de Instrumentao e Fsica Experimental de Partculas — LIP, Lisboa, Portugal

<sup>d</sup>Faculdade de Cincias, Universidade de Lisboa, Lisboa, Portugal

<sup>e</sup>Dep. Fsica and CEFITEC of Faculdade de Ciencias e Tecnologia, Universidade Nova de Lisboa, Caparica, Portugal

<sup>f</sup>CERN, Geneva, Switzerland

<sup>g</sup>DESY, Hamburg and Zeuthen, Germany

<sup>h</sup>Niels Bohr Institute, University of Copenhagen, Kobenhavn, Denmark

<sup>i</sup>Institute of Nuclear Physics Polish Academy of Sciences, Krakow, Poland

<sup>j</sup>II Physikalisches Institut, Justus-Liebig-Universit Giessen, Giessen, Germany

<sup>k</sup>Faculty of Mathematics and Physics, Charles University in Prague, Praha, Czech Republic

<sup>l</sup>Department of Physics, Humboldt University, Berlin, Germany

E-mail: [Karl-heinz.hiller@desy.de](mailto:Karl-heinz.hiller@desy.de)

<sup>1</sup>Corresponding author.

<sup>2</sup>Deceased.

**ABSTRACT:** The ATLAS Roman Pot system is designed to determine the total proton-proton cross section as well as the luminosity at the Large Hadron Collider (LHC) by measuring elastic proton scattering at very small angles. The system is made of four Roman Pot stations, located in the LHC tunnel in a distance of about 240 m at both sides of the ATLAS interaction point. Each station is equipped with tracking detectors, inserted in Roman Pots which approach the LHC beams vertically. The tracking detectors consist of multi-layer scintillating fibre structures read out by Multi-Anode-Photo-Multipliers.

**KEYWORDS:** Large detector systems for particle and astroparticle physics; Particle tracking detectors; Performance of High Energy Physics Detectors; Scintillators and scintillating fibres and light guides

---

**Contents**

|          |   |           |
|----------|---|-----------|
| <b>1</b> | <b>Introduction</b>                         | <b>1</b>  |
| <b>2</b> | <b>Detectors</b>                            | <b>2</b>  |
| 2.1      | Concept and technology choice               | 2         |
| 2.2      | Scintillating fibres                        | 3         |
| 2.3      | Main Detectors                              | 3         |
| 2.4      | Overlap detectors                           | 3         |
| 2.5      | Trigger counters                            | 4         |
| 2.6      | Detector assembly                           | 4         |
| 2.7      | Fibre position survey                       | 6         |
| 2.8      | Roman Pots and related surveys              | 6         |
| 2.9      | Photo-detectors                             | 8         |
| <b>3</b> | <b>Front-end electronics</b>                | <b>9</b>  |
| 3.1      | Motherboard functions                       | 11        |
| 3.2      | Triggerboard functions                      | 11        |
| <b>4</b> | <b>Detector performance</b>                 | <b>11</b> |
| 4.1      | Light yield                                 | 12        |
| 4.2      | Fibre layer efficiency                      | 13        |
| 4.3      | Cross talk                                  | 14        |
| 4.4      | Spatial resolution                          | 15        |
| 4.5      | Edge sensitivity and distance measurement   | 16        |
| <b>5</b> | <b>Experimental setup</b>                   | <b>17</b> |
| 5.1      | Roman Pot stations                          | 17        |
| 5.2      | Positioning system                          | 18        |
| 5.3      | Calibration of the positioning system       | 20        |
| <b>6</b> | <b>Detector Control System</b>              | <b>21</b> |
| <b>7</b> | <b>Trigger and data acquisition systems</b> | <b>21</b> |
| 7.1      | Trigger system                              | 22        |
| 7.2      | Data acquisition system                     | 23        |
| <b>8</b> | <b>Operation experience and upgrades</b>    | <b>24</b> |
| 8.1      | Beam-based alignment                        | 24        |
| 8.2      | Radiation measurements                      | 25        |
| 8.3      | Impedance measurements                      | 26        |
| 8.4      | Temperature measurements                    | 26        |
| 8.5      | Upgrades for Run 2                          | 26        |
| <b>9</b> | <b>Summary</b>                              | <b>29</b> |

---

## 1 Introduction

This article describes all aspects of the ALFA detector which is part of the ATLAS [1] experiment at the LHC. The ALFA detector was constructed in order to give ATLAS the possibility to detect elastically scattered protons, and to some extent also diffractively scattered protons, in the very forward direction. Elastic scattering and diffractive physics have an interest in itself. However, elastic scattering in the very forward direction can also be used to measure the total cross section,  $\sigma_{\text{tot}}$ , and the luminosity,  $L$ , at a collider. Actually the acronym ALFA stands for **Absolute Luminosity For ATLAS** [2]. Traditionally, measurements of  $\sigma_{\text{tot}}$  and the luminosity, using elastic scattering, have been done at every new hadron collider since the time of the ISR [3–5].

The optical theorem connects the total cross section,  $\sigma_{\text{tot}}$ , to the elastic scattering amplitude,  $f_{\text{el}}$ , and states:

$$\sigma_{\text{tot}} = 4\pi \text{Im}[f_{\text{el}}(t = 0)] \quad (1.1)$$

where  $f_{\text{el}}(t = 0)$  is the elastic scattering amplitude in the the forward direction and  $t$  is the four-momentum transfer. The use of the optical theorem requires thus measurements at very small  $t$ -values in order to reduce the model-dependent impact from the extrapolation to  $t = 0$ . Measuring very small  $t$ -values means in turn measuring the protons at very small angles. A special LHC beam optics is needed for this purpose. The beam has to be more parallel than normally and as the divergence goes as  $1/\beta^*$  special runs with a high  $\beta^*$ -optics are needed.<sup>1</sup> To be sensitive to small angles it is necessary to place the detectors far away from the interaction point and close to the beam.

Usually Roman Pots [6] have been used at all  $pp$  or  $\bar{p}p$  colliders to position detectors very close to the circulating beam. A Roman Pot is basically a vessel for detectors that is connected to the accelerator vacuum via bellows. Such an arrangement allows the detector to approach the beam very close without entering the machine vacuum.

It is of importance that the detector inside the Roman Pot adds only a minimal amount of insensitive material towards the beam to avoid acceptance losses at small  $t$ -values. ATLAS has chosen to equip the Roman Pots with tracking detectors based on scintillating fibres. This option has two advantages: the fibres are sensitive up to their physical edge, and they cannot interact with induced electro-magnetic noise from the circulating beams.

The ALFA detector was used in LHC Run 1 and, after some upgrades, also in Run 2. Run 1 was the first data taking period of LHC from 2009 to 2013 followed by Run 2 starting in spring 2015.

The paper is organized in the following way: the construction of fibre detectors, trigger counters, Roman Pots and the photo-detectors is outlined in section 2. The front-end electronics is described in section 3. In section 4 the detector performance measured in test beam campaigns is summarised. The experimental set-up in the LHC tunnel and the positioning system are discussed in section 5. Section 6 deals with the Detector Control System. The triggering and data acquisition systems are described in section 7 while operation experience and upgrades are discussed in section 8. Finally, a summary is given in section 9.

---

<sup>1</sup>The  $\beta$ -function determines the width of the beam envelope around the ring and depends on the focusing properties of the magnetic lattice. The value at the interaction point is denoted by  $\beta^*$ .

## 2 Detectors

### 2.1 Concept and technology choice

The design of the ALFA detector is driven by the goal to precisely measure the track of scattered protons at millimetre distance from the LHC beams. This is achieved by placing detectors in Roman Pots (RPs), i.e. thin walled vessels which allow to operate the detectors inside the LHC beam pipe. The physics requirements demand a detector resolution of about  $30\ \mu\text{m}$  in both coordinates transverse to the beam direction with a uniform efficiency up to the detector edge. Furthermore, for precise alignment, the distance between the upper and lower detectors needs to be measured. An Overlap Detector (OD) was built to get this quantity with a precision of  $10\ \mu\text{m}$ .

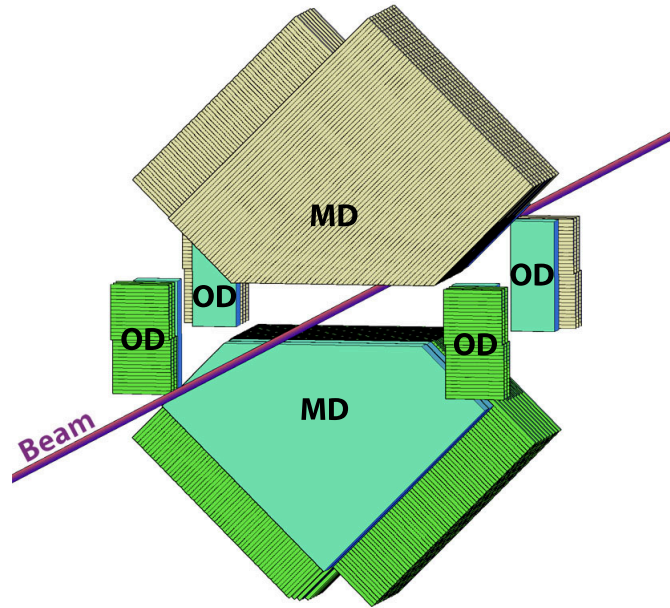


**Figure 1.** A sketch of the detector principle: MD labels the main detectors above and below the beam while OD stands for the overlap detectors. The lines across MDs and ODs indicate the orientation of the scintillating fibres. The areas without a fibre structure mark the trigger tiles. Copyright CERN: reproduction of this figure is allowed as specified in the CC-BY-4.0 license.

The ALFA tracking detectors are based on staggered layers of square-shaped scintillating fibres, read out by Multi-Anode Photo-Multiplier Tubes (MAPMTs). As illustrated in figure 1, the fibres of the Main Detectors (MDs) are inclined by  $\pm 45^\circ$  with respect to the vertical direction. The sensitive region has the shape of a truncated square. In the ODs the fibres are arranged horizontally measuring the vertical coordinate only.

The scintillating fibre technology has some advantages: the signals are of optical nature which provides a maximum immunity to pick-up Radio Frequency (RF) noise from the pulsed LHC beam, it does not dissipate any power which facilitates the operation under vacuum, the detector edge facing the LHC beam is fully active and the staggered multi-layer structure allows to tune the resolution to the needs. On the other hand, the use of scintillating fibres at a hadron collider is a challenge. Organic scintillators provide limited hardness to ionising radiation and, particularly for

small diameter fibres, the small signal amplitudes demand more effort to assure a high and uniform efficiency.

## 2.2 Scintillating fibres

The scintillating fibres, used in the MDs and ODs are of the blue-emitting type.<sup>2</sup> They are square-shaped with outer dimensions of  $0.5 \times 0.5 \text{ mm}^2$  and have a single  $10 \mu\text{m}$  cladding. The signals have the typical fast decay time of organic scintillators, 2.8 ns. The optical attenuation of the signal along the fibre is described by the superposition of two exponential functions  $\exp(-x/\Lambda)$  with  $\Lambda = 120 \text{ cm}$  and  $160 \text{ cm}$ , respectively, and plays a secondary role given a fibre length of about 35 cm. To minimize cross talk of primary ultraviolet scintillation light between the closely packed fibres, the side faces are coated with a 100 nm reflective aluminium film.<sup>3</sup> In order to maximize the light signals for the photo-detectors, the  $90^\circ$  end faces of the fibres are mirror coated by sputtered aluminium. Due to the machining of the fibre modules, as described in section 2.6, a large fraction of fibres was cut at  $45^\circ$  and lost the reflective end face. However, more than half of the light arrives to this end face beyond the critical angle of total reflection and is sent back to the MAPMTs.

## 2.3 Main Detectors

Each MD consists of ten fibre modules with two layers of 64 orthogonally arranged fibres. These modules exist in ten flavours with layers staggered in steps of a tenth of the fibre size. Ignoring the inactive cladding material, the theoretical resolution of a single layer of  $0.5 \text{ mm}$  square fibres is  $0.5 \text{ mm} / \sqrt{12} = 144 \mu\text{m}$ . Provided all ten layers are precisely staggered and fully efficient, such an arrangement is in principle capable to provide a resolution of  $14.4 \mu\text{m}$ . The fibres are tilted by  $\pm 45^\circ$  with respect to the vertical coordinate. This arrangement avoids that inactive cladding material forms a dead zone at the detector edge. Another practical side effect is that routing the fibres towards the MAPMTs does not require too small bending radii. The details of the assembly procedure are described in section 2.6. The various metrology activities for the fibre modules, the detectors and the RPs are documented in sections 2.7 and 2.8. A complete ALFA detector is shown in figure 2.

## 2.4 Overlap detectors

Each OD consists of three fibre layers with 30 fibres each, which are staggered in steps of a third of the fibre size. Due to the limited space inside the RPs, the routing of the fibres towards the photo-detectors requires a bending by  $90^\circ$  with radii  $\leq 20 \text{ mm}$ . To assure the integrity of the fibres they were pre-bent at a temperature of  $85^\circ\text{C}$ . The ODs are fixed to the same support structure as the MDs, described in section 2.6. They exceed the edge of the MDs in the vertical direction by about 9 mm. Consequently, the active areas of the ODs begin to overlap when the upper and lower MDs approach closer than 18 mm. The distance can be calculated from a large sample of particles traversing the overlap region of upper and lower ODs. The OD positions with respect to MDs were calibrated in test beam measurements described in section 4.

<sup>2</sup>Kuraray SCSF-78, specification at <http://Kuraraypsf.jp/>.

<sup>3</sup>Vacuum coating by physical vapour deposition.

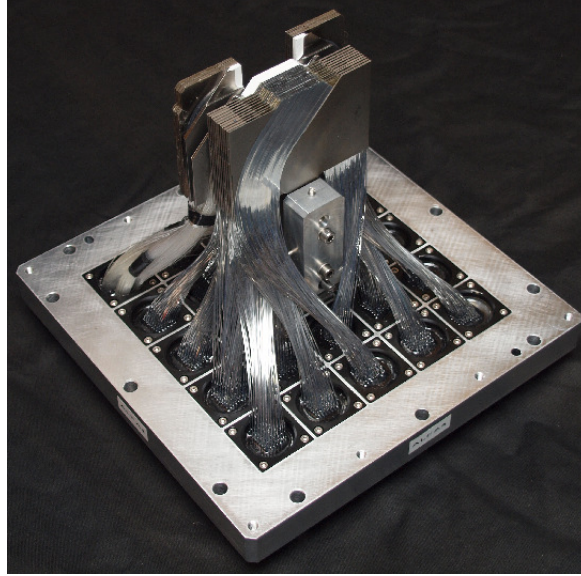


**Figure 2.** An ALFA detector, comprising ten MD modules, three OD modules and the trigger counters coated with white reflective paint in between. The scintillating fibres are routed to plastic connectors in the grid of the base plate which on the other side is facing the MAPMTs. The four bundles of clear fibres for the readout of the trigger tiles are routed to the connector in the upper left hole of the base plate.

## 2.5 Trigger counters

Both, MDs and ODs, are equipped with scintillator tiles for triggering. They are made of 3 mm thick standard plastic scintillator and read out via bundles of clear plastic fibres of 0.5 mm diameter.<sup>4</sup> The MDs are equipped with two trigger tiles which have the shape of the sensitive detector area. The ODs have single trigger tiles with a size of  $15 \times 6 \text{ mm}^2$ . To maximise the light yield and suppress optical cross talk all trigger tiles are covered by white reflective paint.<sup>5</sup> The signals of the trigger tiles are fed into the trigger system described in section 7.

## 2.6 Detector assembly

The assembly of the MD fibre modules proceeded in several steps as illustrated in figure 3. A titanium plate with precisely machined  $45^\circ$  angles for the fibre positioning served as a base substrate. To facilitate the gluing of the fibres a G10 sheet with lithographic pattern was glued between the two angles of the titanium plate filling the empty space of the fibre crossing area.<sup>6</sup> On each side of the substrate 64 fibres were sequentially positioned starting from the  $45^\circ$  precision angles. In their final positions the fibres were fixed by several auxiliary wedges and clamps, the module was turned and the other side assembled by the same procedure. Then the module was brought in an upright position and the gluing process started by immersion of the fibre ends in a tank of glue. The glue dispersed by capillary effect in the small gaps between the substrate and the fibre stack. Before completion of polymerization the fibre ends were removed from the tank. The excess of glue was

<sup>4</sup>Bicron BC-408 or ELJEN EJ-200.

<sup>5</sup>Bicron BC-600.

<sup>6</sup>G10 is a fibre glass epoxy composite laminate.



removed and in the area where the fibres are not supported by the G10 plate an acryl sheet was inserted to ease the subsequent machining of this edge. In the final step of the gluing procedure the fibres in the crossing area were kept straight by corresponding wedges shown in figure 3. Outside of the crossing area the fibres were bent to meet the connectors towards the MAPMTs. The 30 fibres of an OD module were glued in batches of 15 fibres to both sides of the titanium substrate. The glue was directly dispersed on the substrate and the fibres were arranged one-by-one on the prepared area fixed with auxiliary wedges.

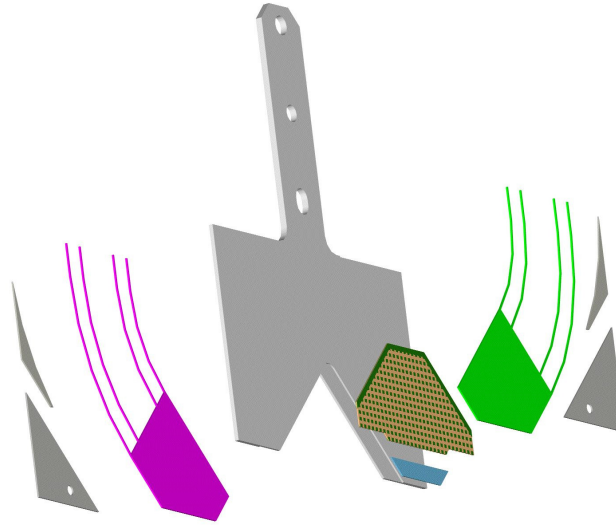


**Figure 3.** Exploded view of the module assembly procedure. The central part (grey) is the titanium substrate with two precision holes for positioning and another hole for the fixation screw. From the inner to outer positions follow the G10 sheet (yellow with green dots), the acryl sheet (blue), two stacks of 64 scintillating fibres (pink, green) and the wedges (grey) to support the fibre routing.

The MD and OD trigger counters were produced by gluing the scintillator tiles on substrates with 0.5 mm lips while ensuring the position of the lower edge by a precision jig. Clear lightguide fibres were assembled to bundles and glued to the scintillator tiles.

After the module assembling the fibre positions were measured by microscope, described in section 2.7. Then the modules were machined at the lower edge to get a distance of 135 mm to the precision hole of the titanium substrate indicated in figure 5.

Next, ten MD modules, three OD modules and three trigger modules were assembled to the full detector composition. They were stacked on two precision pins of the central support arm which is attached to the detector base plate. The support arm has adjustable elements to optimize the clearance of the detector to the RP walls and to optimize the distance to the inner RP bottom window. It also incorporates a cable feedthrough for temperature probes and Light-Emitting Diodes (LEDs). A schematic 3D view of the module structure is shown in figure 4.

Finally, the scintillating fibres were routed to the feedthroughs in the base plate and inserted in the connector holes. The connector bowl was filled with glue and after polymerization the side facing the MAPMT was machined with a diamond tool and polished to ensure a good optical contact.

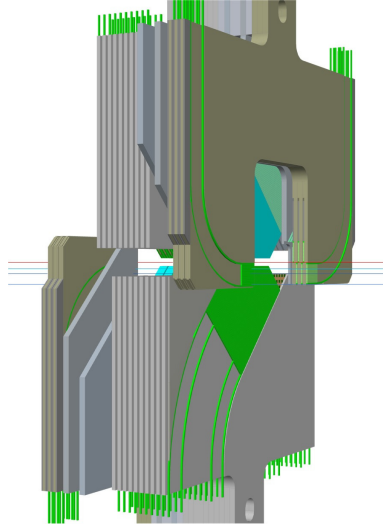


**Figure 4.** A schematic sketch showing the composition of fibre and trigger modules in an upper and lower RP. From outside to inside: three OD modules (dark grey), the OD and MD trigger counters (blue) and ten MD modules (light grey). The sensitive areas of the upper and lower ODs overlap at both sides of the MDs. The small gap between the upper and lower MDs ensures the passage of the LHC beam.

## 2.7 Fibre position survey

The resolution of multi-layer fibre detectors depends on the staggering of the individual layers. The staggering value of each layer is determined by the position of the first fibre attached to the precision groove of the titanium substrate. Due to effects of machining precision and deviations of fibre widths from the design value, the fibre positions differ from the nominal values. The impact on the detector resolution can be partly compensated if the real fibre positions are used for the track reconstruction. For this purpose all fibre positions were measured by a 2D microscope.<sup>7</sup> The measurement scheme for the MD fibre substrates is shown at figure 5. From the gap positions at both fibre edges along the lines A to E, the central values were calculated and fitted to straight lines. The deviations from the nominal fibre positions depend on the fibre number and differ along the measured lines. They can accumulate up to a few 100  $\mu\text{m}$  and are specific for each substrate. The measurement scheme for the OD substrates is based on the same principle.

## 2.8 Roman Pots and related surveys

The RP houses the detector and therefore its design takes into account the constraints imposed by the detector geometry as well as the compatibility with the movement system of the station. A RP is shown in figure 6. It consists basically of a cylindrical pot with special caverns for one MD, both ODs and two flanges. The circular flange is connected to the bellow which is attached to the LHC vacuum chamber and allows the movement of the RP. The squared flange is used to fix the detector base plate with the feedthroughs to the MAPMTs and trigger Photo-Multiplier-Tubes (PMTs). The RP is mostly made of 2 mm stainless steel. The side walls perpendicular to the beam were machined to 0.5 mm thickness and the RP bottom window was reduced to 200  $\mu\text{m}$ . At the

<sup>7</sup>Nikon DS-5M Digital Camera.

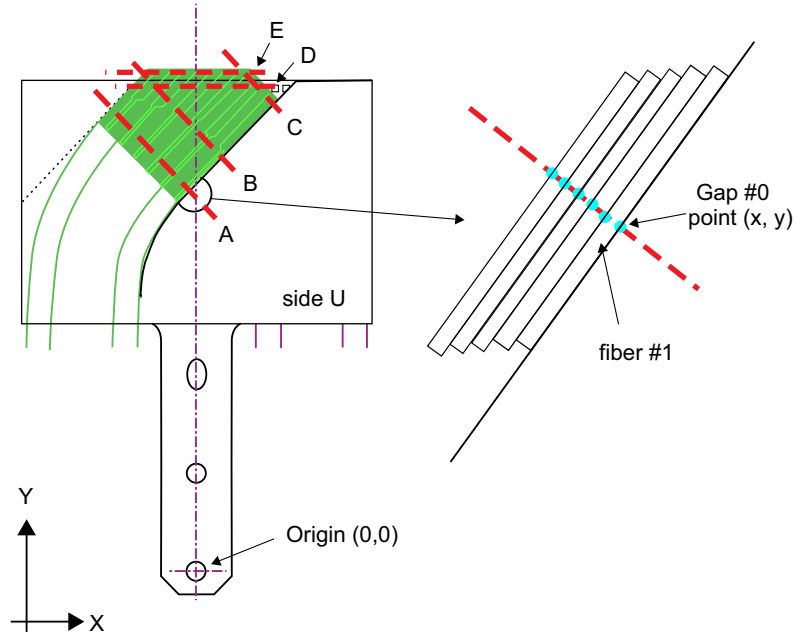


**Figure 5.** Sketch of a fibre substrate with the lines A to E where the gaps between the fibres are measured. The detector coordinate system is defined by the precision hole (0, 0) and the long hole towards the fiducial detector area.

bottom of the cylindrical part of the RP a semi-circular ferrite tile is attached. It aims to absorb the electro-magnetic power of the RF losses related to the impedance of RP cavities. Although the fibres themselves are insensitive to electro-magnetic radiation, the RF losses result in a heating of the titanium plates where the fibres are glued. This heating effect and preventing measures are described in section 8.3.

Due to the thin  $200\ \mu\text{m}$  RP bottom window the protection of the ultra-high LHC vacuum is a major safety aspect. For this purpose and to minimize the deformation induced by the atmospheric pressure on the window the interior of the RP is kept in a secondary vacuum. Pumps close to the stations keep the pressure below 20 mbar. Pressure tests have shown that the thin RP bottom window withstands overpressure up to 80 bar before destruction. Since the maximum encountered overpressure in case of an accidental loss of the secondary vacuum would be 1 bar the ultra-high LHC vacuum is well protected. To maintain the secondary vacuum all fibre feedthroughs of the base plate which closes the RP need to be carefully sealed by glue in the last step of the assembling procedure described in section 2.6. For the precise positioning and to ensure the necessary clearance all RPs and detectors were surveyed with a mechanical 3D measuring device with a precision of about  $5\ \mu\text{m}$ .<sup>8</sup> The distance to the RP bottom window was measured at five positions close to the corners and in the centre. A small outward bend of about  $50\ \mu\text{m}$  was observed at the central position.

Before the detectors were assembled, all fibre modules were measured and grouped in batches with similar module length. After assembling a final 3D measurement of the lower detector edge was performed.

For a typical detector the results are shown in figure 7. The trigger tiles, which are covered by white reflective paint of thickness between  $20\ \mu\text{m}$  and  $40\ \mu\text{m}$ , are slightly protruding. To ensure

<sup>8</sup>Olivetti Inspector MAXI 900V.

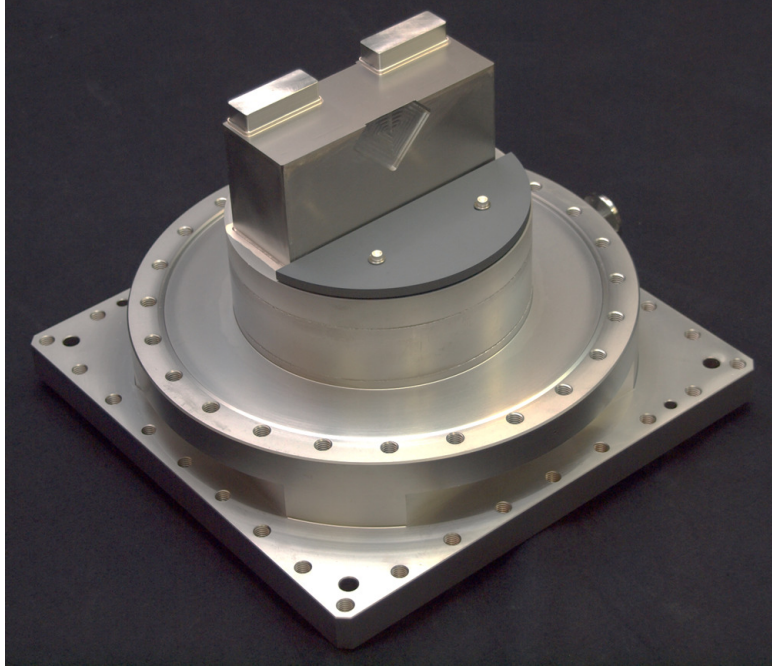


**Figure 6.** A photo of a bare Roman Pot. In uppermost positions extending the bottom window are the two extrusions for the ODs. At the side wall the front window machined to the sensitive MD area is visible. The ferrite tiles are attached to the cylindrical RP bottom. The square flange which is foreseen to hold the detector has outer dimensions of  $264 \times 264 \text{ mm}^2$ .

an optimal gap between the lower detector edge and the inner RP bottom window, the detector fitting best in each individual RP was selected. All gaps range between  $150 \mu\text{m}$  and  $250 \mu\text{m}$ . Under vacuum conditions, the expected bend of the base plate which carries the detector is in the order of  $40 \mu\text{m}$ , reducing the gap by this amount. Before the insertion of the detectors in the RPs the clearance to the inner RP walls was adjusted by small screws impacting the angles of the detectors on the holding arm. The typical clearance was between  $0.5 \text{ mm}$  and  $1 \text{ mm}$ , in a few extreme cases reduced to a few  $100 \mu\text{m}$ .

## 2.9 Photo-detectors

The MAPMT technology, a reliable and proven technology, fulfills all requirements for the readout of a relatively large number of scintillating fibres. The chosen device provides an  $8 \times 8$  grid of channels with a nominal pitch of  $2.3 \text{ mm}$ , including  $0.3 \text{ mm}$  gaps for separations of the sensitive readout pixels, which is adequate for the readout of  $0.5 \text{ mm}$  square fibres.<sup>9</sup> Even though the cross talk between direct channels is small, the fibres were routed such that neighbouring fibres were not read by neighbouring MAPMT channels. The typical quantum efficiency is  $26\%$  and the gain is in the order of  $10^6$  at a bias of  $-1000 \text{ V}$ . However imperfections of the micro-machined dynode channels lead to channel-to-channel variations of a factor 2–3. The average gains of different MAPMTs can differ by a similar factor.

<sup>9</sup>Hamamatsu R7600-00-M64, specification <http://www.hamamatsu.com/>.

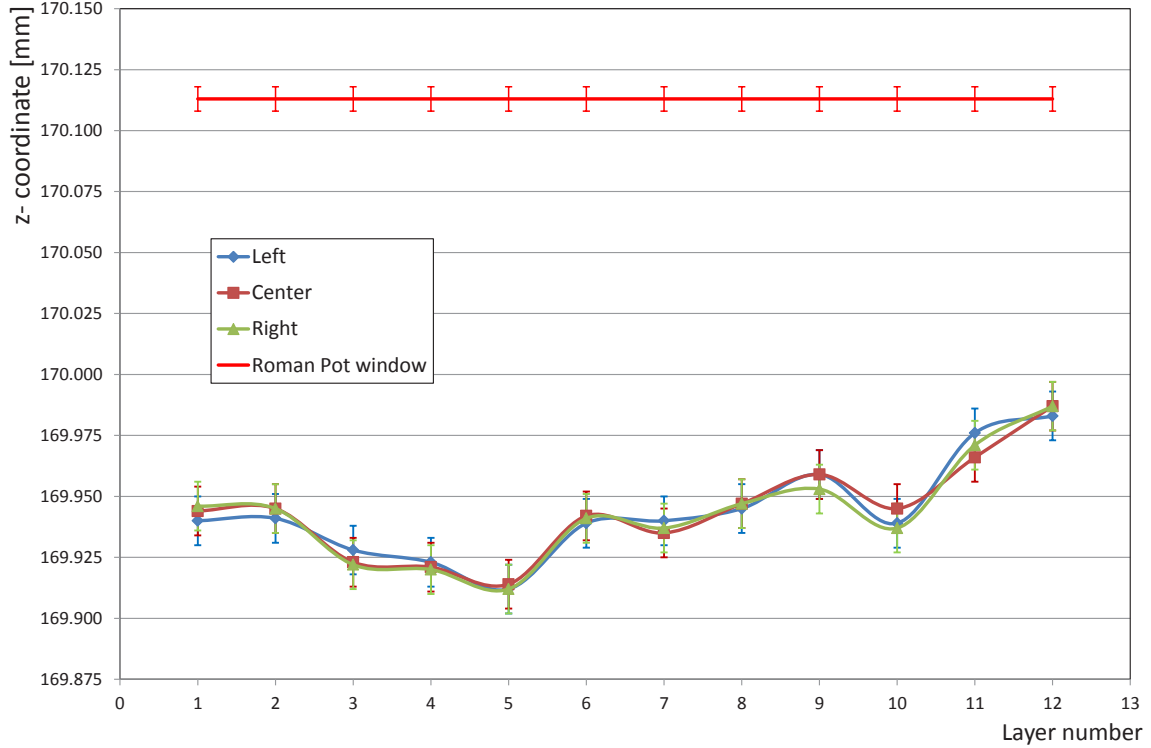


**Figure 7.** The positions of the lower edges of the MD modules (1–10), the MD trigger tiles (11–12), and the inner RP window (red line) are indicated with respect to the RP flange. For all modules three values are quoted: in left, central and right positions along the lower detector edge.

For technical reasons, the internal dynode structure is displaced by about 1 mm relative to the tube centre. The displacement can be obtained from alignment marks on the first dynode and corrected for by gluing plastic shims on the MAPMT bodies. Due to its compact size, this MAPMT operates in the earth magnetic field without any shielding. In view of possible stray fields in the LHC tunnel, all MAPMTs as well as the trigger PMTs are protected by a mu-metal grid which is integrated in the base plate structure, described in section 2.6.<sup>10</sup>

The scintillator tiles of the trigger counters are read out by 8 mm diameter miniature PMTs of the metal package type. For the MD trigger tiles a PMT with super-bialkali photo-cathode is used which offers a peak quantum efficiency of 35%.<sup>11</sup> The OD trigger tiles, where the detection efficiency is less critical, are read out by a PMT with conventional bialkali photo-cathode.<sup>12</sup>

### 3 Front-end electronics

The front-end electronics is fitted in a tight volume on top of the ALFA stations. The timing, control and data communications are sent over more than 240 m to the Detector Control System (DCS) and Data AcQuisition system (DAQ) with adapted techniques to ensure the data rate and the latency

<sup>10</sup>A nickel-iron soft magnetic alloy with very high permeability suitable for shielding against magnetic fields.

<sup>11</sup>Hamamatsu R9880U-110, specification <http://www.hamamatsu.com/>.

<sup>12</sup>Hamamatsu R7400P, specification <http://www.hamamatsu.com/>.

of the first level trigger (L1) decision. The high voltage biasing lines are deployed along the LHC tunnel and through local patch panels at the stations connected to the MAPMTs or trigger PMTs. Each electronics assembly receives two low voltage power lines (5 V, 10 A and 7 V, 1 A) delivered from local power units, placed close to the stations in a service alcove to avoid excessive voltage drops through the cables.

The Photo-Multiplier Front-end electronics (PMF) is a compact stack of three boards connected directly to the backplane of each MAPMT. The first board provides the high voltage distribution to the dynodes of the MAPMT. A transition board is equipped with contact sockets for the MAPMT pins and passes the signals to the third board that holds the analogue Multi-Anode ReadOut Chip (MAROC) and a digital readout Field-Programmable Gate Array (FPGA). A PMF attached to the MAPMT backplane is shown in figure 8.



**Figure 8.** A side view of a MAPMT with a stack of three boards, the PMF, which performs the readout of the fibre signals.

In the 64-channel MAROC chip [7], the MAPMT signals are pre-amplified, shaped with 15 ns shaping time and fed into a programmable discriminator. The global threshold and gain settings per channel are configured through the local FPGA from the ALFA DCS. The MAROC provides also a 110 ns slow shaper followed by a sample and hold and a multiplexer circuit that can be activated to read the analogue charge per channel. Due to the multiplexing time, the analogue charge readout is operational at a low rate of a few kHz and was used only for tests. The MAROC 64 discriminator outputs are fed into the FPGA where they are continuously sampled at 40 MHz, the LHC bunch crossing rate. The sampled data are buffered in a pipeline until the centrally processed L1 trigger signal arrives. With the L1 decision the digital data of the associated bunch crossing are transmitted through a 40 MHz serial interface to another FPGA located on the motherboard, which collects the data from all 23 PMFs per detector. The general layout of the fibre front-end electronics is shown in figure 9.



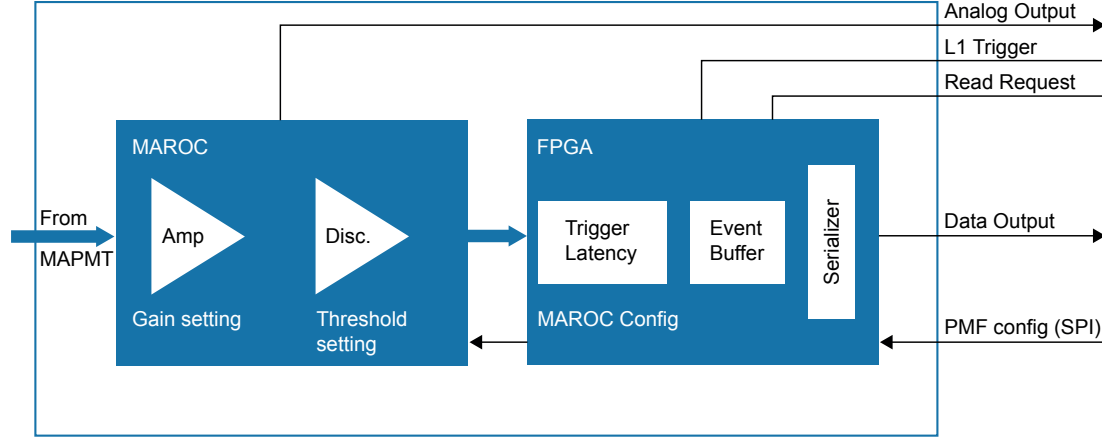


**Figure 9.** The architecture of the front-end electronics for the readout of the fibre signals from the MAPMTs, as it is realised in the PMF.

### 3.1 Motherboard functions

The motherboard receives the clock, trigger and command signals from the central ATLAS Timing, Trigger and Control (TTC) system through an optical link. It controls all communication with the 23 PMFs per detector. After the L1 decision the PMF data are formatted to the event structure defined for the MROD modules of the ALFA branch of the DAQ system, described in section 7.2. The data are transmitted at 1.2 Gb/s by a fast serialiser, a gigabit optical link [8], and an optical driver. The motherboard functions, and all the front-end electronics elements, are controlled and monitored by an Embedded Local Monitoring Board (ELMB) interface card [9] which is connected to the ALFA branch of the DCS.

### 3.2 Triggerboard functions

The triggerboard is mounted as a mezzanine on top of the motherboard. The four signals of the trigger PMTs, two from the MD scintillator tiles and two from the OD scintillator tiles, are pre-amplified, shaped and discriminated by two MAROC chips. The binary output of the MAROCs is fed into a FPGA that is configured to perform various combination of the four trigger signals. The output signal is sent to the counting room to contribute to the L1 decision in the Central Trigger Processor (CTP), as outlined in section 7.

The triggerboard supports two programmable pulse generators, designed to deliver variable amplitudes (up to 4 V) and short pulses (5 to 50 ns range) to the two LEDs installed inside each RP. The LEDs are placed close to the scintillating fibres and used to generate test signals to verify the readout system.

## 4 Detector performance

A series of test beam measurements were carried out to assess the performance of the ALFA detectors. In 2005 the principle of a scintillating fibre tracker was demonstrated [10]. In 2010 all but one detector were inserted in two RP stations equipped with the final version of the front-end electronics. To optimize the performance data sets with different detector parameters were analysed.

The 2010 beam test was performed in the H6B area of the H6 beam line of the CERN SPS North Area with a 120 GeV hadron beam. For precise tracking the EUDET silicon pixel telescope [11] was used. It consists of six sensors layers with an internal space point resolution of  $4.5 \mu\text{m}$  covering an active area of  $21.2 \times 10.6 \text{ mm}^2$ . The ALFA stations with the fibre detectors were placed about 1 m downstream of the EUDET telescope. At this distance the pointing precision for tracks reconstructed in five or more pixel layers ranged from  $3 \mu\text{m}$  to  $5 \mu\text{m}$ .

Since the transverse area of the EUDET sensor was smaller than the area of the fibre detectors, a position scan in vertical and horizontal directions was performed. A typical track pattern where the beam hits the edges of the upper and lower MDs is shown in figure 10. The tracks reconstructed by the EUDET telescope were used to measure the distance between the detector edges.

In the next sections the following performance parameters are documented: the light yield of the scintillating fibres and of the trigger scintillators, the hit multiplicities and related layer efficiency, the cross talk, the spatial resolution, the edge sensitivity and the position calibration of the ODs. The quoted values are based on optimized detector settings for high-voltages, gains and thresholds as they are used later for LHC data taking.

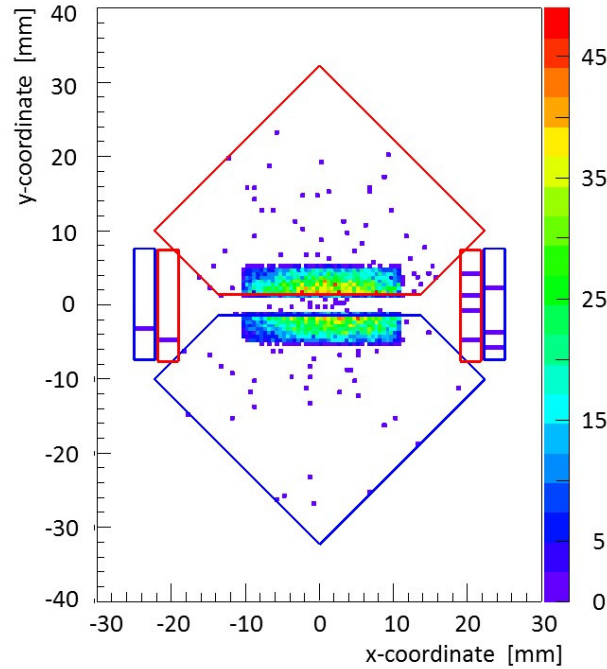


**Figure 10.** A track pattern with the beam in central position on the station. The distance between upper and lower RPs was about 2 mm. The size of the track pattern is defined by the lateral size of the EUDET trigger counters. At both sides of the MDs the ODs are symbolised.

#### 4.1 Light yield

A high light yield is a key parameter to ensure a good tracking quality. The first measurements based on a module of  $2 \times 32$  fibres were performed in a DESY test beam with 6 GeV/c electrons [10]. Later, the fibres of all detectors were exposed to cosmic particles to calibrate the amplifiers and equalize the signal amplitudes for discrimination [12].



Before the cosmic exposure each fibre channel is illuminated at low light level from a pulsed LED to determine the mean amplitude  $x_1$  and the width  $\sigma_1$  of the 1 Photo-Electron (PE) signal. With the known 1 PE parameters the amplitude spectrum  $Q(x)$  of cosmic particles can be described by a Poisson distribution  $P(i, \mu)$  convoluted with the Gaussian functions of all  $i$  PE signals as described by formula (4.1):

$$Q(x) = A \sum_{i=0}^n P(i, \mu) \cdot e^{-(x-x_i)^2/2\sigma_i^2}. \quad (4.1)$$

The mean amplitude and the width of the  $i$ -th PE term are parametrised by the 1 PE signal:  $x_i = i \cdot x_1$  and  $\sigma_i^2 = \sigma_0^2 + i \cdot \sigma_1^2$ , respectively. The sum in (4.1) is cut off at  $n = 15$  PEs. The fit provides the overall normalization factor  $A$ , the mean amplitude and the width of the pedestal,  $x_0$  and  $\sigma_0$ , and the average number of  $\mu$  PEs.

A striking difference to the beam data is the angular distribution of incident cosmic particles. This results in two effects which need to be corrected for an estimate of the light yield of beam particles traversing the detectors under  $90^\circ$ : a cosmic particle can deposit more energy per fibre due to the inclined trajectory, and for the same reason it can cross more than one fibre. Simulations have shown that the first effect increases the light yield by a factor 1.2, while the second effect enlarges the cross talk by about 20%.

The light yield of a typical fibre layer exposed to cosmic particles is shown in figure 11. For the fibres with the aluminium coated end faces the yield is about 5 PEs, while for fibres which lost the coating by machining it is 0.5 PE to 1 PE less. The average light yield of all layers varies by  $\pm 1$  PE. The cross talk generated by inclined trajectories is at the level of 1 PE. For the light yield of the OD fibres similar results were obtained. According to Poisson statistics a light yield of 4 PEs allows a single fibre efficiency of 98%.

For the trigger tiles different coatings and light guide version were investigated in a DESY test beam with 6 GeV electrons [13]. The best results were achieved with tiles covered by white reflective paint read out by flexible bundles of round light guide fibres of 0.5 mm diameter. The measured light yield was about 40 PEs.

## 4.2 Fibre layer efficiency

For each charged particle passing a fibre layer one would expect exactly one fibre hit. Due to secondary interactions in the surrounding detector material, electronic noise and cross talk the average multiplicity per layer is larger. Dependent on the position where the beam hits the detector the values range between 1.05 and 1.27 hits per layer. To measure the layer efficiency the trajectories of beam particles were reconstructed from hits in all layers excluding the layer under inspection. For a typical MD the layer efficiency with the beam incident to the central detector area is shown in figure 12. The average value of 93.5% degrades slightly along the particle path through the detector due to losses by secondary interactions. Also shown in figure 12, the layer efficiency varies as a function of the incident beam position from 92% to 94%, with a typical spread of about 1% among the detectors. These values are in good agreement with the expectations taking into account efficiency losses due to the  $10 \mu\text{m}$  insensitive cladding material ( $-4\%$ ) and the 1 PE amplitude threshold ( $-2\%$ ) for the digitisation.

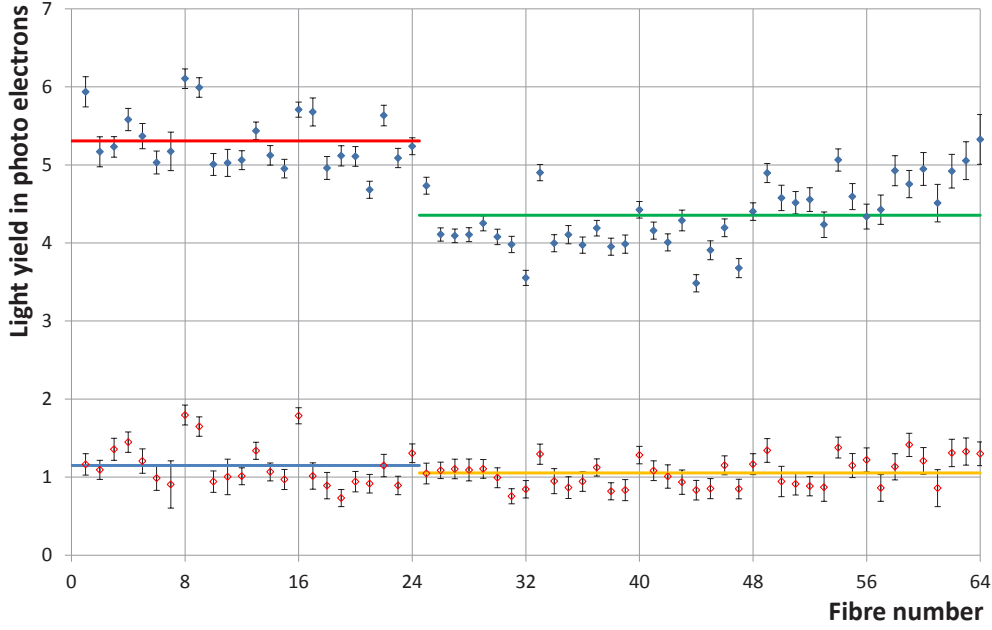


**Figure 11.** The light yield of a layer of 64 fibres in terms of PEs. The fibres 1–24 have a reflective aluminium end face, while the fibres 25–64 were cut and lost the reflective end. The lower data points describe the cross talk contribution due to inclined cosmic particles traversing neighbouring fibres.

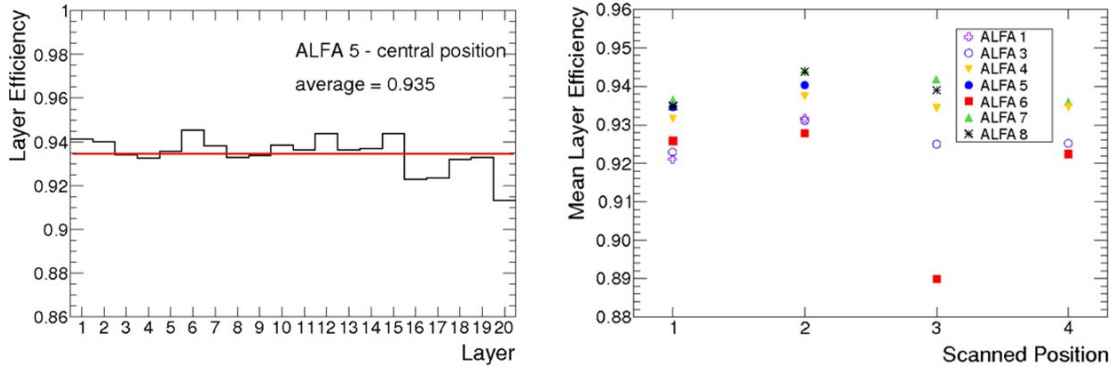


**Figure 12.** Left: the layer efficiency of the ALFA5 detector with the beam focused to the central detector area. Right: the layer efficiency of the ALFA1–8 detectors scanned at four positions — the central detector area (1), the lower detector edge (2), the left (3) and the right (4) detector corners. Apart from an outlier (ALFA6 at position 3) all values are centred at the average with a maximum spread of  $\pm 1\%$ .

### 4.3 Cross talk

Cross talk in adjacent fibres or MAPMT channels fakes signals which degrade the performance of a tracking detector. The first measurement of cross talk was based on the early DESY data [10]. Later, measurements with cosmic particles and SPS test beams were done with final detectors and front-end electronics. The mapping of fibres to MAPMT channels was optimized to reduce the impact of cross talk on the track reconstruction. The evaluation of cross talk is based on hit counting, while the early DESY data were analysed using amplitude information. Due to these

differences, the later SPS test beam results are a more realistic estimate of the performance under LHC conditions.

The relative amount of hits in fibres aside the reconstructed particle track is shown in figure 13. It results from the superposition of four types of cross talk: the direct fibre cross talk, the MAPMT cross talk, and the cross talks attributed to neighbouring connector and MAROC channels. The fibre cross talk amounts to an average value of 6% and is a mixture of two components: 2% for the fibres with coated end faces and 8% for the fibres without coating due to the 45° machine cut. The latter enhanced value is attributed to light exiting the fibres towards the RP bottom window in about 200  $\mu\text{m}$  distance where it is reflected into the neighbouring fibres with uncoated end faces. To reduce these reflections the inner RP windows were subsequently covered by an anti-reflective paint which reduces the amount of reflected light by factors between three and five.<sup>13</sup>

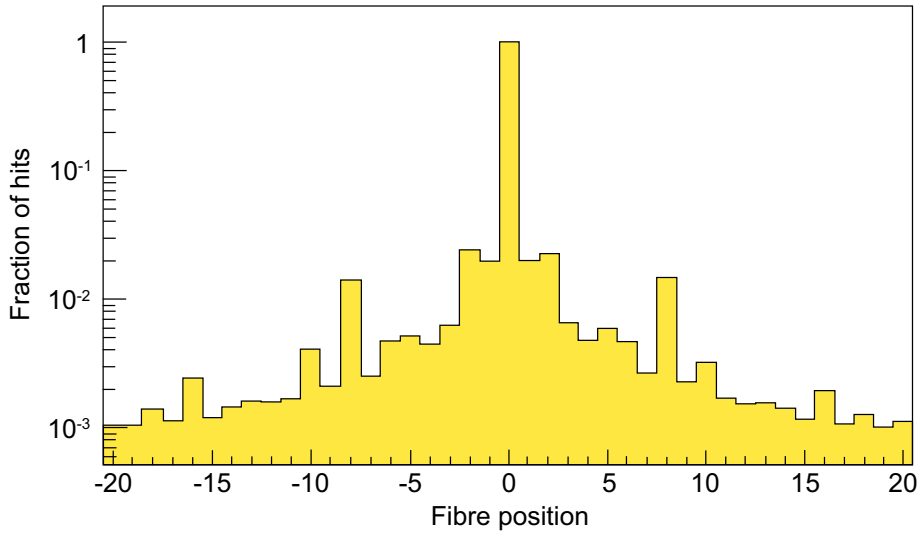


**Figure 13.** Distribution of fibre hits with respect to the position of the particle trajectory. The structure with peaks at various positions, e.g. at  $\pm 8$  fibres, results from the MAPMT cross talk in combination with fibre-to-MAPMT mapping scheme.

The cross talk in neighbouring MAPMT channels is about 4.5% for the direct neighbours and 1% for the diagonal neighbours. According to the fibres-to-MAPMT mapping scheme, the cross talk in direct MAPMT channels enhances the amount of hits in a distance of two, eight or ten fibres with respect to the genuine track hit, visible in figure 13. The cross talk related to the MAROC chip and connectors contributes at the level of 2% each.

The various cross talks are the dominant source of noise hits which contribute to the hit multiplicity per layer, described in section 4.2.

#### 4.4 Spatial resolution

The spatial resolution was measured by extrapolating the tracks reconstructed by the EUDET telescope to the position of the MDs. The uncertainty of this extrapolation was about 5  $\mu\text{m}$  if at least five pixel layers were used. The track reconstruction in the MDs is based on the overlapping of

<sup>13</sup>Deflocculant Acheson Graphite.

fibres which are attributed to the particle trajectory. For this purpose the measured fibre positions, described in section 2.7, are used. The central value of the overlap area is used as the position where the particle passed the MD. The difference between track coordinates reconstructed in the fibre detector and the positions predicted by the EUDET telescope is used to determine the spatial resolution. Since the contribution of EUDET to the convoluted resolution is negligible, these plots quantify the resolution of the MD.

Various effects degrade the theoretical resolution noticed in section 2.3. The most relevant contributions are:

- The measured fibre positions (section 2.7) deviate from their design values, sometimes up to a few 100  $\mu\text{m}$ . This deteriorates the layer staggering which is a condition for the ideal resolution.
- The fibre layer efficiency (section 4.2) is not 100% due to the non-scintillating cladding around the fibre core and the amplitude cut for the digitisation of the fibre signal.
- The cross talk reduces the primary fibre signal and generates hits at outlying positions (section 4.3).
- Physics processes like Coulomb scattering or generation of  $\delta$ -electrons affect the particle trajectory or generate signals in the neighbouring fibres.

The measured spatial resolution of all MDs ranges between 30  $\mu\text{m}$  and 40  $\mu\text{m}$ .

#### 4.5 Edge sensitivity and distance measurement

The reconstruction of the incident beam particle trajectories by the EUDET telescope allows a tomography of the fibre detectors inserted in the RPs. The trigger condition requires a coincidence between the EUDET trigger counters, which cover the size of the pixel sensors, and the trigger counters of the MD fibre detectors described in section 2.5. The vertical projection of the beam trajectories with a corresponding trigger signal is shown in figure 14. In most cases the beam particle passes the EUDET telescope and the fibre detectors without interactions. The related track pattern indicates the lower (upper) edge of the upper (lower) MD trigger counter and the outer edges of the EUDET trigger counters. If the beam hits the RP bottom windows interactions generate shower particles which are scattered into the upper or lower MD trigger counters. The track pattern of these events shows the position of the upper and lower RP bottom windows as indicated in figure 14.

The tomography pattern allows to measure positions inside the RP which are not accessible by other measuring equipment. For this purpose the edges of the pattern were fit with smeared step functions defined individually in the ranges where the hit counts rise steeply. The width of the smearing is about 20  $\mu\text{m}$  and results from small differences of the size, the roughness and the reflectivity of individual trigger modules. Some discontinuities visible at the positions of the windows are resulting from the beam profile and the slight convex shape of the RP windows, discussed in section (2.8). The essential values from the fit are the positions of the MD edges and their distances to the RP bottom windows. For all combination of MDs and RPs the distance varies from 150  $\mu\text{m}$  to 250  $\mu\text{m}$ . The fit confirmed the window thickness of 200  $\mu\text{m}$  obtained by machining of the RP bottom surface. The distance between upper and lower MD edges changes with the RP

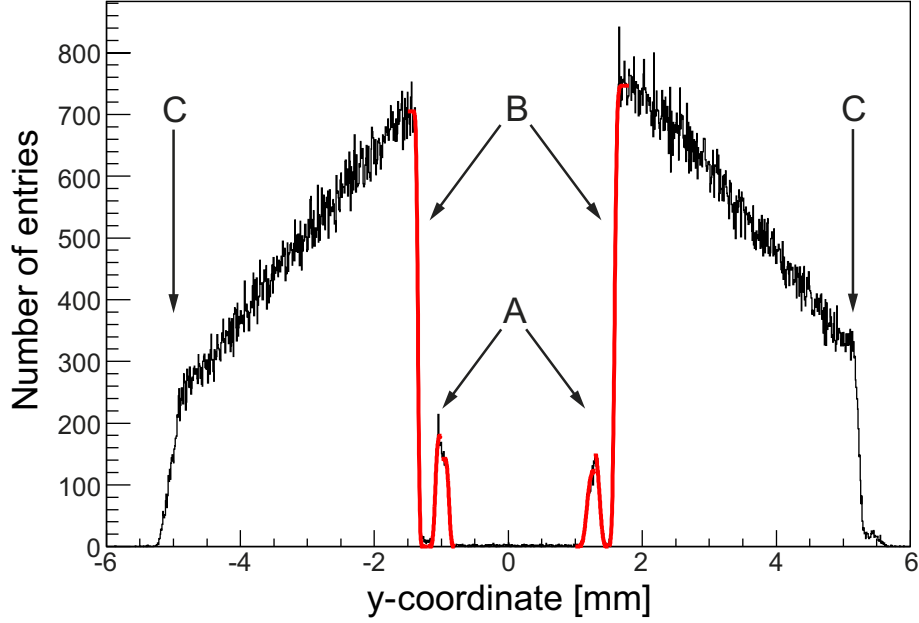


**Figure 14.** A vertical tomographic cross section of a RP station with upper and lower MDs. Clearly visible are the RP bottom windows (A) and the lower MD edges (B). At values of  $\pm 5$  mm (C) the histogram is cut by the size of the EUDET trigger counters.

movement. For the case shown in figure 14 the distance between the upper and lower RP outer window faces was set to about 2 mm.

Another important task of the test beam campaign was the calibration of the OD fibre positions with respect to the MD coordinate system. For this purpose the MD coordinate system was aligned to the EUDET reference system. Then the OD fibre positions were scanned by EUDET tracks and compared with the values measured by microscope, described in section 2.7. The differences are in the order of  $100\ \mu\text{m}$ , and vary among all ODs. Applying corresponding corrections, the OD distance measurement differs less than  $10\ \mu\text{m}$  from the direct values given by the edges of upper and lower MDs.

## 5 Experimental setup

The ALFA system consists of four stations each equipped with two detectors in an upper and lower RP. Two stations are placed in a distance of about 240 m at both sides of the ATLAS interaction point, in the long straight LHC sections. The distance between two stations was approximately 4 m during Run 1; it has been increased to 8 m for Run 2 to improve the angular resolution. The positions as well as the naming scheme of the stations are indicated in figure 15. This section is split into three subsections describing the main station components, the movement system and the calibration of the movement system.

### 5.1 Roman Pot stations

The stations have been designed to satisfy the strict requirements of positioning precision and all aspects of the LHC operation, complying with ultra-high vacuum, impedance, temperature,

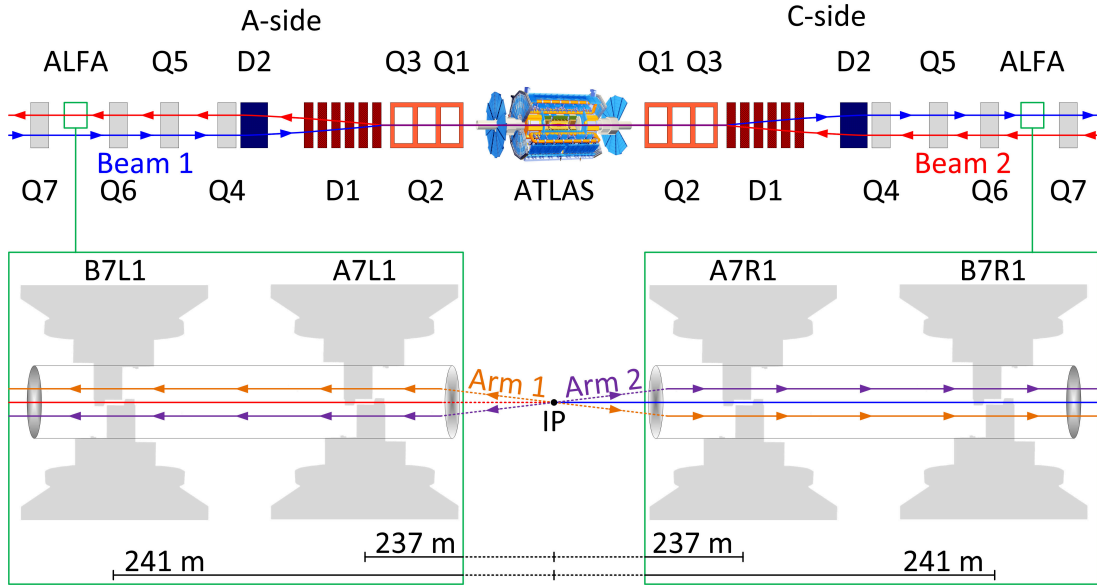


**Figure 15.** A schematic view of the LHC beam lines up to the ALFA stations with the relevant magnets. The lower part indicates the station names and their positions in Run 1. Copyright CERN: reproduction of this figure is allowed as specified in the CC-BY-4.0 license.

electricity and safety constraints. The detectors inside the RPs and the readout electronics are physically separated from the LHC vacuum.

Each station is composed of a stiff main body and two RP flanges which can be moved vertically by step motors, described in section 5.2. The upper and lower flanges, which carry the RPs, are connected by flexible bellows to the beam pipe. The bellows are connected to the LHC vacuum chamber and allow an excursion of 50 mm towards the beam. A station in the assembling hall is shown in figure 16.

Each station is equipped with a compensation system to counterbalance the atmospheric pressure on the RP and to ensure auto-retraction. It consists of two additional bellows placed at the backside of the station as shown in figure 16. The compensation bellows are connected by lever arms to the RP bellows on the other side and balance the atmospheric pressure. Due to the larger size of the compensation bellows, the force on the RP bellows which pulls them with 2.7 kN towards the beam is over-compensated by a outwards force of 3.6 kN. This ensures an auto-retractile movement in case of power loss. The first station B7L1 was installed in the winter shutdown 2009 while the other three followed one year later.

## 5.2 Positioning system

The station allows an independent movement of the upper and lower RPs via a high precision roller screw moved by a step motor. The main components of the positioning system are the radiation hard motors, the rotary position sensors mounted on the motors, the Linear Variable Differential Transformers (LVDTs), and the switches and stoppers to control the movement range. Some details are listed in the following bullets:



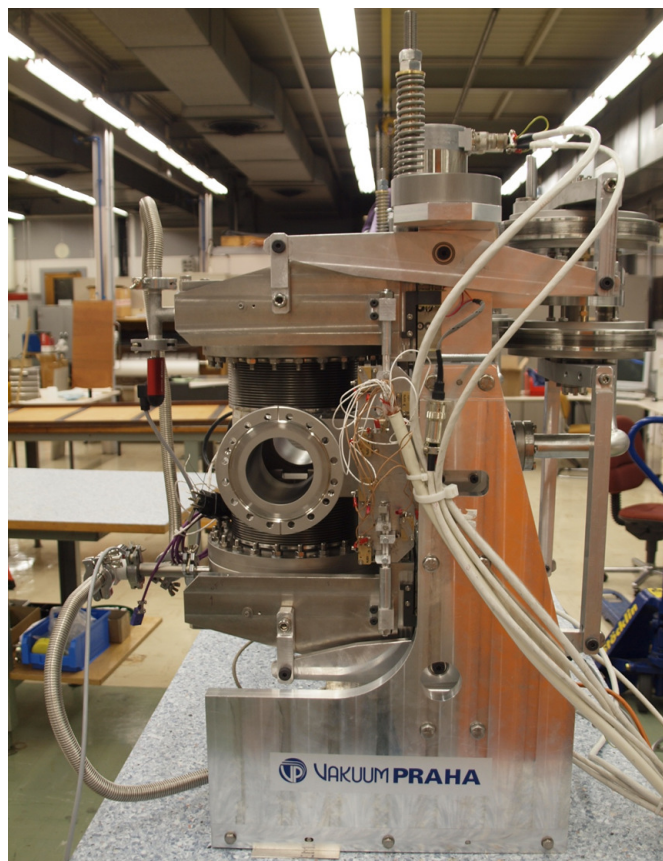


**Figure 16.** A side view of a RP station in the lab. On the left side of the station body the round flange of the beam pipe, the upper and lower RP bellows and the RP flanges are visible. A lever arm with a pivotal point at the upper part of the station body connects the RP flanges with the squeezed compensation bellows at the upper backside of the station. On top of the station two springs are mounted which support the auto-retraction. In between the springs the step motor of the upper RP is installed. On the right side of the beam pipe flange the plate with the micro-switches is fixed.

- The motors are expected to cope with an integrated radiation dose of 30 MGy. In operation, one revolution corresponds to 400 motor steps,  $5\text{ }\mu\text{m}$  each. The expected lifetime of the motors is 15 million revolutions.
- Contactless resolvers have been selected as rotary position sensors due to their capability to withstand high radiation doses. Although the resolvers were installed right from the beginning, they were operational only in Run 2.
- The LVDTs are used to measure the RP position with respect to the centre of the beam pipe. The position reproducibility is about  $10\text{ }\mu\text{m}$  in periods of a few days when the data runs are performed. In the long term larger drifts were observed. Due to the high radiation environment, the readout electronics is placed outside the tunnel.
- The movement range of each RP is defined by an inner and outer electrical stopper. The outer stopper serves as reference to follow the stability of the position values. To protect the

motors against movement beyond the hard end-points, micro-switches are placed in millimeter distance after the stoppers. Accidental collision of the upper and lower RPs are blocked by an anti-collision switch. The system of micro-switches and stoppers is shown in figure 17.

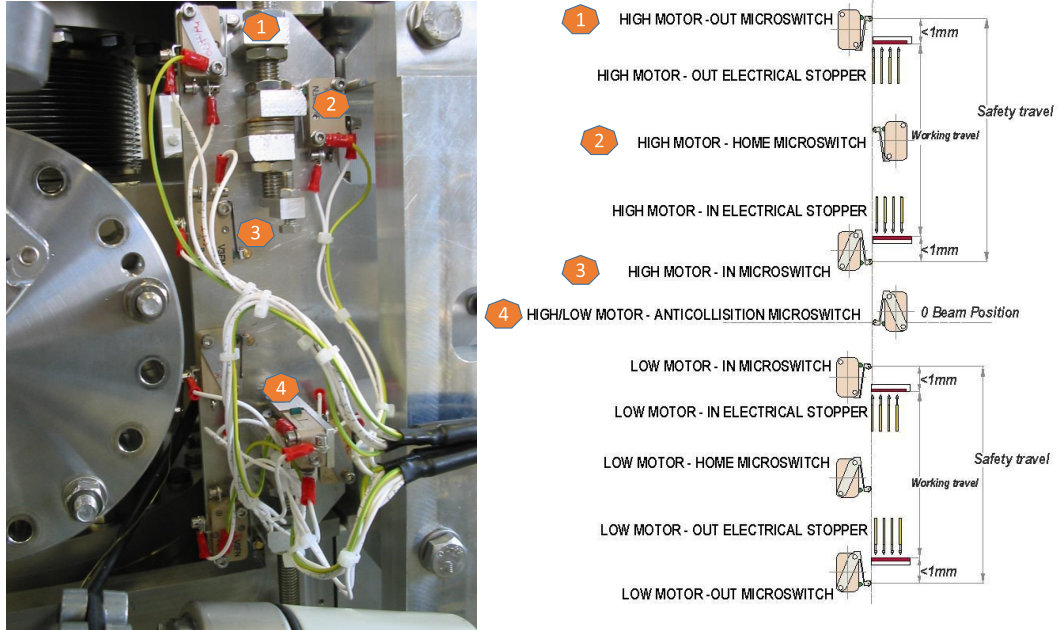


**Figure 17.** The picture on the left side shows the practical implementation of the micro-switches attached to the RP station. The positions can be adjusted by means of screws and washers. On the right side the schematic layout of all components is shown.

### 5.3 Calibration of the positioning system

After the installation of the stations in the LHC tunnel the RP movement system was calibrated by a laser survey.<sup>14</sup> First, the coordinate system was defined by measuring the outer contours of the RP station. Next, moving the RPs inwards the LVDT current ratio was recorded in steps of 2 mm (1 mm close to the beam centre) along the movement range. To include angular effects, the RP positions are derived from three laser targets which are fixed to the RP base plates. The position of these targets were measured in the laboratory by a 3D device.<sup>15</sup> Combining the 3D survey of the targets with the laser survey in the tunnel the LVDT current ratio is used to determine the absolute position of the RP bottom window with respect to the centre of the beam pipe. To get rid of fluctuations, typically in the order of 10–20  $\mu\text{m}$ , the RP positions as a function of the LVDT current ratio was parametrised by a third order polynomial. As the LVDTs, also motor steps and resolvers were calibrated by the laser survey.

The largest uncertainty on the RP positions results from the limited visibility of the contours defining the station coordinate system. Including the contributions from the 3D surveys of the RPs and the laser targets, it is in the order of 100  $\mu\text{m}$ . The position recording from the LVDTs, the

<sup>14</sup>Leica LDT500, Leica Geosystems Inc., Norcross, U.S.

<sup>15</sup>TESA Micro-hite 3D CMM.



motor steps and the resolvers are used for the beam-based alignment before data taking, described in section 8.1.

## 6 Detector Control System

The Detector Control System (DCS) is responsible to control and to monitor all relevant detector parameters using a Finite State Machine (FSM), to perform the alert handling and the data archiving. The local ALFA DCS server with a SLC6 Linux operation system is connected to the global ATLAS DCS which handles all ATLAS sub-detectors [14].

The front-end electronics is configured by sending appropriate parameter values to the FPGAs of the PMFs. Parameters like gains, thresholds, control bits, trigger patterns, rates, latency have a direct impact on the data quality. Other detector parameters like currents, voltages, temperatures, RP positions, etc. need to be followed for hardware failures. If they are outside a normal range an alarm is triggered and propagated through the FSM alerting the operation team to take measures that assure the data quality.

Some detector components are directly handled through the Linux server, others which are accessible only by a Windows interface are connected to a virtual machine with a Windows operation system. The ELMBs [9] for the configuration of the detectors, the temperature and radiation monitoring, the control of the VME crate with the DAQ related front-end hardware and the controller of the low voltage power supply are directly connected by CAN-USB interfaces to the Linux server. The virtual Windows machine controls through CAN bus connections the high-voltage power supplies, and through Ethernet connections the RP vacuum pumps and the fans for the air cooling. The RP movement control is integrated in the LHC system and performed by two specific computers.<sup>16</sup>

A cutout of the ALFA DCS top panel is shown in figure 18. Various sub-panels allow to access individual detectors or infrastructure components to configure or retrieve parameters.

## 7 Trigger and data acquisition systems

The signals of all eight MD trigger counters, described in section 2.5, are discriminated, amplified and shaped in the triggerboards, referred in section 3.2, and fed into the Central Trigger Processor (CTP). Different combination of the eight input signals are used to select physics or background processes. The main trigger for elastic events consists of coincident signals from the upper detectors at ATLAS side A and the lower detectors at side C, and vice versa. To select diffractive events coincidences of both upper or lower detectors either at side A or side C are used. In addition, various trigger items were defined combining signals from other ATLAS sub-detectors or higher level objects like jets in coincidence with ALFA trigger signals. For the data readout two main chains were used: one with the data of all ATLAS sub-detectors for physics analyses and another only with ALFA data for systematic studies. In the second chain the small event size of about 5 kB allows high rates with looser trigger conditions which are useful for detector performance studies.

<sup>16</sup>A National Instruments PXI which hosts the front-end real time application and a FESA server for the distributed information management.

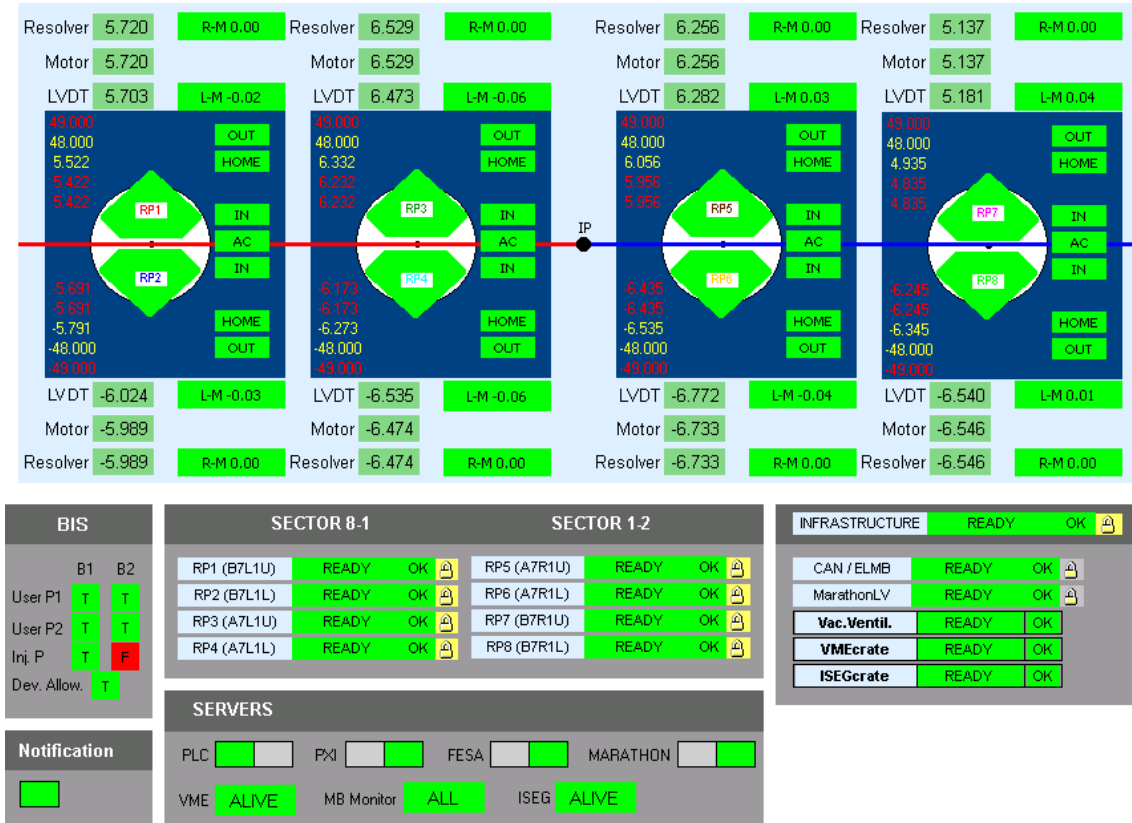


**Figure 18.** A cutout of the ALFA DCS top panel with the RP positions retrieved from the LVDTs, the motor steps and the resolvers. The lower part indicates the status of the Beam Interlock System (BIS), the power status of all detectors in sectors 8–1 and 1–2, the status of the infrastructure components and of all servers. The snapshot is from the  $\beta^* \approx 90$  m run in October 2015 with RP positions at  $10\sigma$  of the beam envelope.

Due to the long distance of about 240 m from the ATLAS counting room the trigger latency is a primary concern. The main contributions to the ALFA latency are the time of flight from the interaction point to the ALFA stations and the signal transmission to the ATLAS CTP with 800 ns and 1030 ns, respectively. To minimize the transmission time special air-core cables which transfer signals with 91% of the speed of light are used.<sup>17</sup> The signal handling in the front-end electronics, the cables and the evaluation of the trigger logic adds up to another 270 ns and brings the ALFA latency beyond the standard ATLAS latency. In the special high- $\beta^*$  runs all ATLAS sub-detectors adapt to the ALFA latency. In the standard LHC low- $\beta^*$  runs ALFA does not participate and the latency change is not needed.

## 7.1 Trigger system

The triggerboard receives the raw trigger signals from the two MD and the two OD scintillator tiles of a detector. Details of the signal handling in the triggerboards are documented in section 3.2.

<sup>17</sup>Andrew Corporation, AVA5-50, HELIAX Coaxial Cable.

The scheme of the standalone trigger logic combining trigger signals from all MDs is shown in figure 19. First a coincidence of the signals from the two MD trigger tiles is requested. The resulting NIM signals are sent through the air-core cables to the central counting room. Here they are split into a CTP and an ALFA standalone branch with three levels of coincidences as indicated in figure 19. The standalone branch provides various options to trigger elastic events and is used for commissioning purposes. The CTP branch with the full spectrum of ATLAS trigger items is used for combined data taking with all ATLAS sub-detectors. The data taking for the distance measurement with the ODs, as described in section 2.4, was performed in standalone mode without the other ATLAS sub-detectors and has therefore not to respect the L1 trigger latency. In 2011 conventional coaxial cables with a transit time of about 1200 ns were used for the signal transfer to the counting room. Since 2012 the OD trigger signals are also transmitted by the fast air-core cables as the MD signals. To distinguish MD and OD trigger signals different signal lengths were attributed to them. The use of the fast air-core cables allows to perform the distance measurement in parallel with the physics data taking.

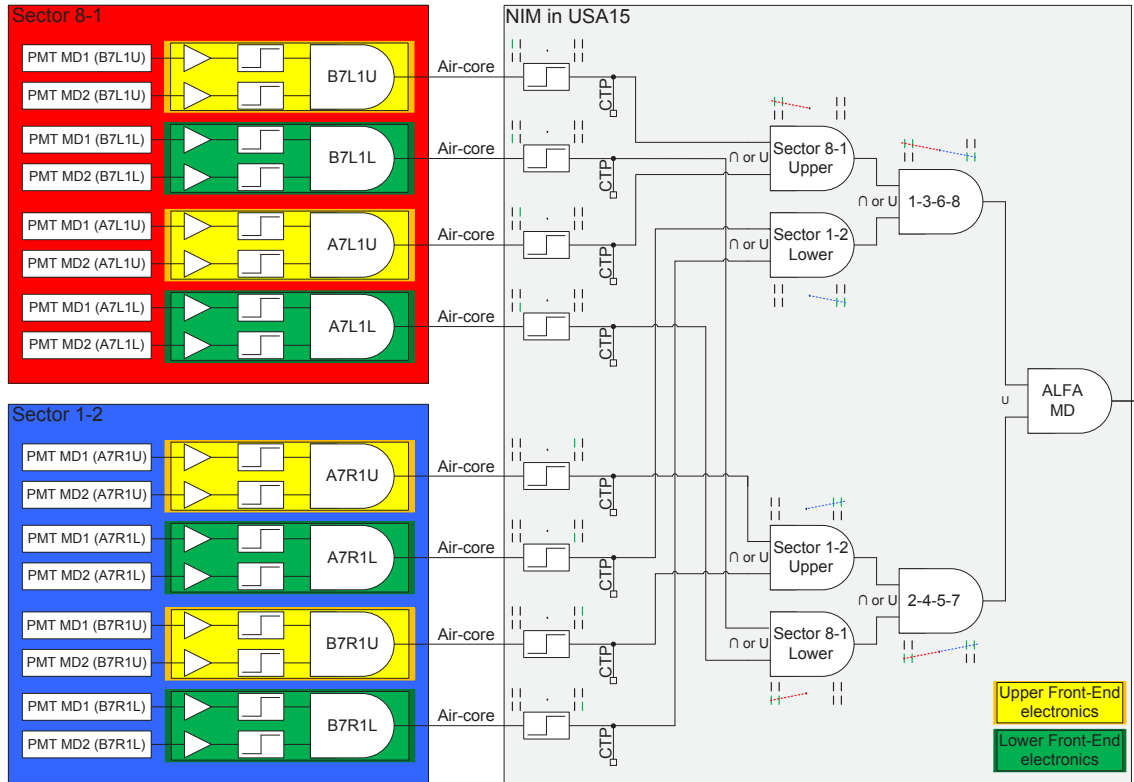


**Figure 19.** The logic scheme of the MD standalone trigger system. The two left boxes contain the local signal handling in the triggerboards at the stations. The right box contains the tree levels of coincidences for the formation of the final trigger signal.

## 7.2 Data acquisition system

At each bunch crossing data from the scintillating fibres are fed into delay pipelines located in the PMFs of the front-end electronics. There they are kept until a L1 trigger decision from the

CTP arrives after a certain latency. In case of a positive decision the data are transferred into the derandomising buffers of the motherboards, otherwise they are dropped. These buffers are the first part of the local DAQ system which provides data aggregation and transfer to the ATLAS-wide ReadOut System (ROS) [15].

The data from the buffers are sent via optical links to the ReadOut Drivers (ROD) which are the ATLAS-wide interface between the detector-specific infrastructure and the ROS computers. ALFA utilizes the Muon ROD modules (MROD) which are designed for the ATLAS muon spectrometer [16]. The MROD module aggregates and frames the incoming data with the L1 event and the bunch crossing numbers. In case of buffer overflow by reception of inconsistent data the module generates a BUSY signal which can stop the ATLAS trigger generation to fix the source of corrupted data.

The MROD module cooperates with another module - the TTC Interface Module (TIM) via a dedicated VME backplane. The TIM module receives L1 and bunch crossing information from the TTC system and broadcasts it to the MRODs. To transfer the data from all detectors two MROD modules are used: one for the two upper detectors from the A-side and the two lower detectors from the C-side, and the other for the mirrored detector composition. Such a connectivity allows to register elastic events within one module and facilitates the online monitoring. Apart from the detector-specific MROD modules, the ALFA readout system utilises ATLAS-wide crate controllers and modules of the trigger and the TTC systems.

The software of the ALFA DAQ is residing on the ROD crate software framework and executed at the controller of the VME crate. It provides all functionality for the control of the MROD modules including configuration and communication at each transition of the DAQ system, i.e. transitions to the configure, start, or stop states of the DAQ. In addition, it allows to acquire data samples from the MRODs via the VME interface. This data can be used for the on-line monitoring of the data quality and give insight into the state of the DAQ system.

## 8 Operation experience and upgrades

After the installation and commissioning phases of the ALFA stations, data taking took place from 2011 to 2013 and was restarted with Run 2 in 2015. In the first part of this section we summarise the experience from alignment of the RPs and the knowledge of the environmental conditions, like radiation levels and temperatures. The second part of the section is about the upgrades implemented during the long LHC break in the years 2013 and 2014. They include improvements of the heat protection, the angular resolution and the trigger performance.

### 8.1 Beam-based alignment

A very precise positioning of the RPs with respect to the beams is mandatory for an optimal data taking and the safety of the LHC machine. This is the aim of the Beam-Based Alignment (BBA). For these procedure the laser-calibrated RP positions, described in section 5.3, have been used. Later, for physics analysis, a track-based alignment is used to determine precisely the MD positions inside the RPs with respect to the beam [17].

In the BBA procedure the RPs are moved towards the beam until the outer RP windows scrape the edge of the collimated beam and induce a spiky signal in the Beam Loss Monitors

(BLMs) downstream of the stations. For the low intensity high- $\beta^*$  runs the BLM dump thresholds were increased by a factor 10 compared to standard running conditions. Close to the beam the movement step size is  $10\text{ }\mu\text{m}$  resulting in a precision of about  $20\text{ }\mu\text{m}$  for the edge of the beam. After the alignment of one station, the beams are reshaped by the vertical primary collimators and the procedure is repeated for the remaining stations.

The BBA procedure is done in a dedicated fill before the data taking with same beam conditions used for the high- $\beta^*$  runs. From the vertical positions of the beam edges the centre and the width of the beam are obtained. These values are used for the positioning of the RPs in the subsequent fill for data taking.

## 8.2 Radiation measurements

For the radiation measurement two different devices have been used: the Thermo-Luminescent Dosimeter (TLD) for integral dose measurement and the Radiation Monitor (RadMon) for on-line monitoring.

Two types of TLDs with different sensitivities were placed at positions compatible with the MDs in parking position: the TLD-100 and the TLD-800 with ranges from  $10\text{ }\mu\text{Gy}$  to  $10\text{ Gy}$  and  $0.5\text{ mGy}$  to  $10^5\text{ Gy}$ , respectively.<sup>18</sup> In periods of about half a year the irradiated TLDs were replaced by fresh ones. After Run 1 the accumulated dose measured by the TLD-100 varied between  $10\text{ Gy}$  and  $30\text{ Gy}$  depending on the detector position.<sup>19</sup> Due to interactions at the inner stations the dose in the outer stations was about 10% to 20% higher. More striking is the 50% dose excess in the upper detectors compared to the lower ones due to the asymmetry of the beam background. The values from the TLD-800 are consistent with the TLD-100 results but are less reliable at such low doses.

The RadMons were installed at various positions around the stations A7L1 and B7L1: two devices close to the detectors (comparable with the TLD positions), one between the beam pipes and three close to the motherboards and the PMFs. They are equipped with two Radiation-sensing Field-Effect Transistors (RadFET) of different sensitivity. In Run 1 only the high-sensitivity RadFETs were used,<sup>20</sup> while in Run 2 at positions with doses above  $5\text{ Gy}$  the readout was switched over to the low-sensitivity RadFETs.<sup>21</sup> The dose values of the RadMons at detector positions confirmed the TLD values with an uncertainty of a few Gy. The RadMons close to the front-end electronics indicated smaller doses at the level of a few Gy.

The radiation hardness of scintillator material is in the range of a few kGy. Dedicated studies made with the fibres used for the ALFA trackers have shown a 10% efficiency loss at  $3\text{ kGy}$ . Hence the dose accumulated in Run 1 is far from a degrading impact on the tracking detectors.

The part of the ALFA detector most sensitive to radiation is the front-end electronics. It is not designed as radiation-hard and sensitive components can start malfunctioning at doses in the order of  $10\text{ Gy}$ .

<sup>18</sup>GC Technology Messgeraete Vertriebs GmbH, Freidling 12, D-84172 Buch am Erlbach.

<sup>19</sup>The TLD dose values are given in units Sv. To convert into units Gy a factor 2 has been used, assuming mainly electro-magnetic radiation with an admixture of hadrons.

<sup>20</sup>LAAS 1600, Laboratory for Analysis and Architecture of Systems, Toulouse, France.

<sup>21</sup>REM TOT501C type K, REM Oxford Ltd., United Kingdom.

### 8.3 Impedance measurements

The installation of the RP stations impacts the LHC impedance budget. In order to avoid the generation of beam instabilities and power deposition to the RPs, heating up the detector, laboratory tests have been performed. A thin wire was stretched through the main chamber of the station and connected to the two ports of a vector network analyser which was used as RF source and signal analyser. This allows to determine the longitudinal and transverse impedance which couples to the LHC beam spectrum. By comparison to a reference signal from a bare beam pipe without the RP caverns the impedance can be calculated. Measurements at various RP positions with different conditions were performed: with the bare RP and with a semi-circular ferrite tile mounted to the RP bottom.

The measurements without ferrite tiles have shown a number of resonances at frequencies between 0.6 GHz and 2.5 GHz. Resonances at low frequencies between 0.6 GHz and 1 GHz are dangerous because they couple strongly to the beam harmonics. The installation of the ferrites reduced the resonances up to 1 GHz significantly. Consequently all RPs were equipped with ferrite tiles, as described in section 2.8.

The RF losses due to the enhanced impedance result in a temperature increase in the material of the stations. The evolution of the temperature during the LHC fills is described in the next section.

### 8.4 Temperature measurements

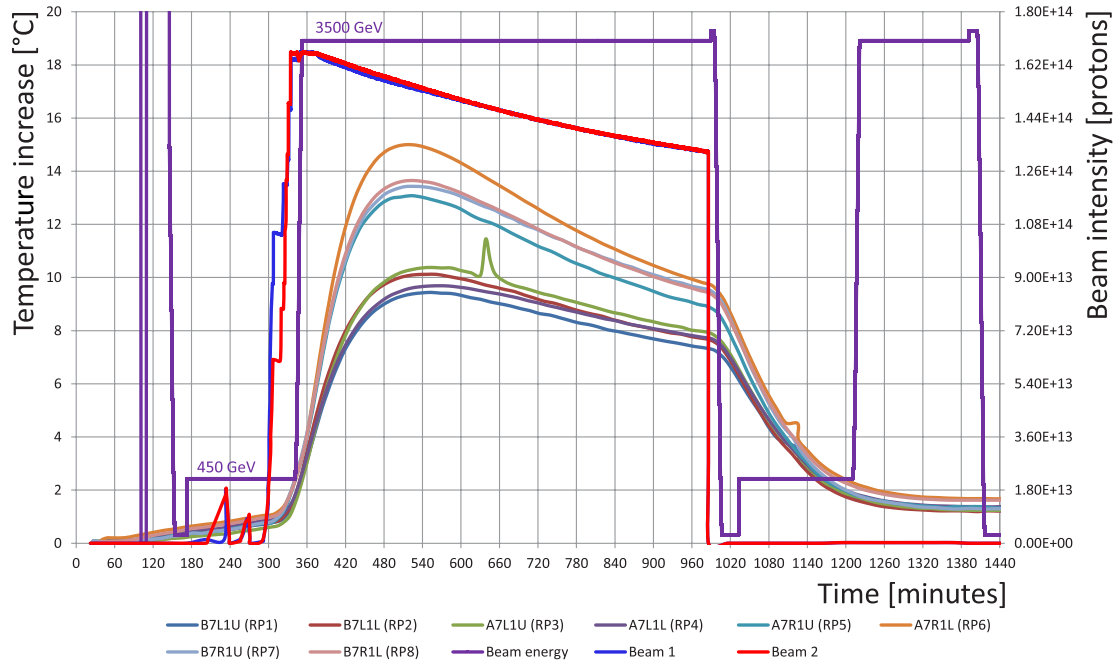
All stations are equipped with temperature sensors at various points of interest, in particular at the front-end electronics, the station body, the RP walls and the titanium substrates of the fibre modules.<sup>22</sup> The sensors are connected to ELMBs and data transferred through CAN bus lines to the central DCS for monitoring.

Figure 20 shows the temperature increase at the titanium substrates of the MDs as a function of the time. Starting at injection of the beam the temperature increase reaches a maximum typically 3 hours after the energy ramp. As expected, the increase is higher at larger beam intensities but depends also on the details of the beam structure. During the standard LHC fills with high beam intensities in Run 1 when the RPs are in garage position, a dangerous temperature increase up to 20° was observed at the titanium substrates where the fibres are glued. Adding the ambient tunnel temperature, at some places up to 25°C, the detectors were heated up to 45°C. The titanium substrates and the fibres glued on them have different thermal expansion coefficients and the resulting stress can destroy the assembly. Laboratory tests have shown that the destructive phase begins at temperatures of about 45°C. The temperature increase was traced back to the RF losses in the cavity housing the RPs with the detectors. Simulation indicated a power deposit of 10 W, which translates into the maximum observed increase of 20°. The modifications to reduce the detector heating are described in the next section.

### 8.5 Upgrades for Run 2

The main effort in the break after Run 1 was dedicated to the heat protection. Extrapolations to Run 2 indicated a power deposit of up to 80 W in case of extreme beam conditions. Other modifications were the displacement of the two outer stations and the improvement of trigger capabilities.

<sup>22</sup>PT100 platinum resistance thermometers.



**Figure 20.** The temperature evolution on the titanium substrates of all RP detectors during a typical fill in Run 1. The individual detectors are labelled by different colour lines. In the peak region the temperature of detectors on the C-side (RP5–RP8) is systematically a few degrees higher compared to the detectors on the A-side (RP1–RP4). The blue and red lines stand for the beam intensities, the purple line for the beam energy.

To minimize the RF impact on the temperature four measures were performed. The most important was to reduce the cavity volume and thereby the RF power deposit by extending the RP by a so-called RP-filler. In addition, the ferrites were mounted at positions further away from the detectors where the wake fields of the beams are absorbed in a more efficient way.<sup>23</sup> Moreover, a heat distribution system made of thin copper plates was installed inside the RP and the air cooling was intensified by additional fans and a better streaming to the RP flanges. The three first modifications are illustrated in figure 21. The RP-filler is made of titanium and connected by conductive copper-beryllium springs for proper grounding to the original RP.<sup>24</sup> The impact of the RP-filler on the resonance lines of the impedance spectrum is shown in figure 22. All resonance lines between 0.6 GHz and 1.8 GHz are strongly reduced. In particular those below 1 GHz, which have the strongest coupling to the beam spectrum and are most dangerous for heating, disappeared completely. The second modification is related to the ferrites with completely revised position and shape. The semi-circular tile attached to the RP bottom has been replaced by a ring of six individual pieces located on the flange, visible in the central section of figure 21. At the new positions the heat is directly emitted to the stainless steel flanges where the air stream for cooling is circulating.

After extensive lab tests, the stations were reinstalled in the LHC tunnel. The temperature increase in a high intensity fill is below 5°, far from the destructive range. Another important effort for Run 2 was the displacement of the outer stations B7L1 and B7R1 downstream from their original positions. In this way the distance between inner and outer station was enlarged from 4 m

<sup>23</sup>Nickel spinel TT2-111, specification <http://www.trans-techinc.com>, Adamstown, MD21710, U.S.

<sup>24</sup>Feuerherdt GmbH, D-12277 Berlin, Germany, <http://feuerherdt.de>.



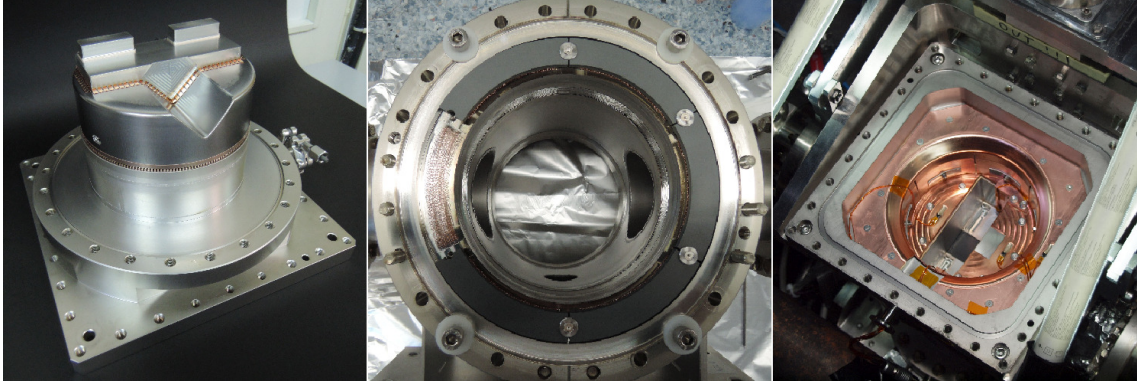


**Figure 21.** Three modifications to improve the heat protection. From left to right: the RP-filler attached to the bare RP, the ring of ferrites distributed on the RP station flange and the copper heat distribution system with attached temperature probes.

to about 8 m. Naturally, the angular resolution was improved by a factor two and results in a higher precision of the derived proton momentum transfer.

The trigger upgrades concerned the dead time and the latency. The reduction of the dead time was achieved by upgrades in the firmware of the MAROC chip of the front-end electronics, described in section 3. It was reduced from 550 ns to 88 ns. This allows triggering and data taking with a bunch spacing down to 100 ns.

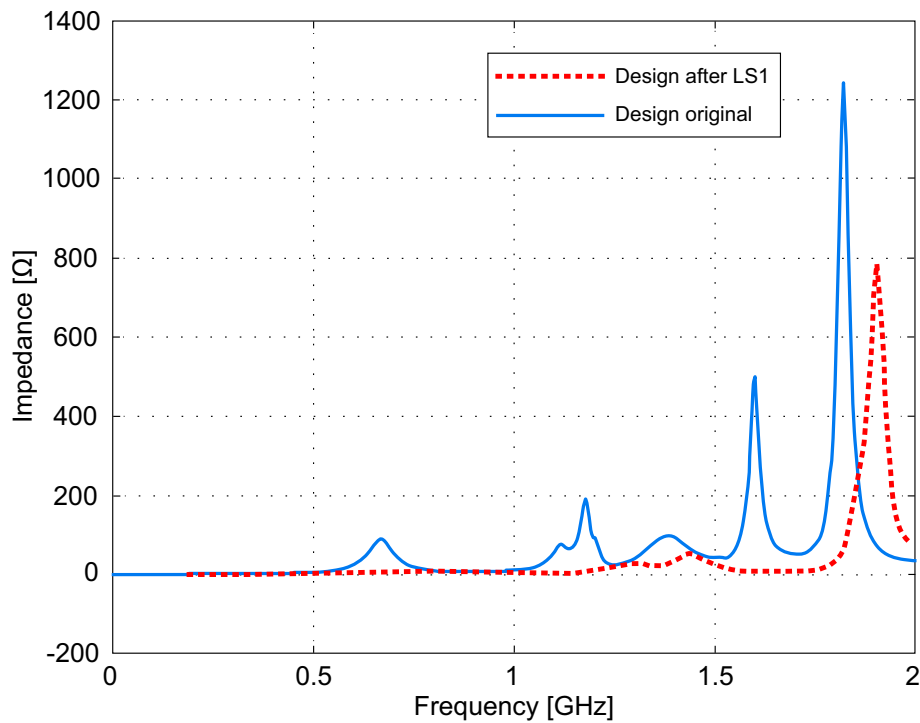


**Figure 22.** The longitudinal impedance as a function of the frequency indicating the coupling strength to the LHC beam spectrum. The blue curve describes the initial RP design, the red curve stands for the modified design with a RP-filler.



The upgrade of the ATLAS CTP for Run 2 brought a latency penalty of about 75 ns what increased the ALFA latency beyond the limits of the L1 trigger budget. For compensation a new back-end triggerboard was produced. It allows to bypass the standard trigger input stages and injects signals directly to the CTP core [12]. In addition, it replaces the NIM electronics used in the past for the separation of MD and OD trigger signals and allows the monitoring of rates per bunch crossing.

## 9 Summary

The construction of the ALFA system and its integration in the infrastructure of the ATLAS experiment is described. Two RP stations are placed at each side of the ATLAS detector at distances of about 240 m. Each station consists of an upper and a lower RP which can be moved towards the beam in vertical direction. The RPs are equipped with tracking detectors to measure forward going protons from elastic or diffractive processes.

The MDs consist of two times ten layers of square  $0.5 \times 0.5 \text{ mm}^2$  scintillating fibres orthogonally arranged perpendicular to the beam. By staggering the individual fibre layers a spatial resolution of about  $35 \text{ }\mu\text{m}$  is achieved. Each layer of 64 fibres is read out by one MAPMT. The typical light yield per fibre is between 4 PEs and 5 PEs what results in a layer efficiency above 90%. For the alignment of the detectors the distance between upper and lower MDs is measured by special ODs which are attached to the MDs. For triggering the detectors are equipped with scintillator tiles. The sensitive area of the main detectors is covered by two 3 mm thick tiles while a single tile is used for the ODs.

The front-end electronics of the fibre readout is directly placed on the back-side of each MAPMT. A dedicated triggerboard receives the signals from the trigger tiles and prepares the transmission to the CTP. If a L1 signal returns, the digitised fibre data are transmitted to the motherboard. Here the event is built and transmitted through an optical link to the ATLAS DAQ system.

The positions of the RPs and their reproducibility are an essential parameters for the physics analysis and the safety of the LHC machine. A precision motor allows the movement of the RPs in steps of  $5 \text{ }\mu\text{m}$  from the garage position towards the beam and vice versa. For the calibration of the RP position a special laser survey was performed. Combining this survey with the 3D measurements of detectors and RPs, the absolute position is known with a precision of about  $100 \text{ }\mu\text{m}$ .

Due to the far position of the detectors the ALFA trigger signals arrive beyond the standard ATLAS latency budget. Fast air-core cables were installed to keep the ALFA latency within the maximum length of the buffering pipeline. Since 2012 also the overlap trigger signals were sent trough the air-core cables to CTP, coded by a different signal length.

To ensure the functionality of detectors and electronics over many years the control of radiation dose and temperature is vital. For dose measurements crystal-based TLDs and electronic RadMons for online monitoring have been used. In Run 1 both sensors indicate doses between 10 Gy and 30 Gy at the detector positions. The temperature was monitored by PT100 elements attached to all relevant parts of the station. A critical temperature increase up to  $45^\circ$  related to the RF losses at high beam intensities was observed with RPs in garage position. Protection against heating was achieved by multiple measures: a RP-filler to reduce the cavity volume, a modified ferrite system, a heat distribution system and an optimized air-stream for the cooling.

The main task of ALFA is the measurement of the proton-proton total cross section at all LHC energies. The results of the Run 1 data taking at 7 TeV and 8 TeV are published [17, 18]. In Run 2 the first data taking at 13 TeV was performed with a  $\beta^* \approx 90$  m optics. Recently, in October 2016, data were taken with an ultra-high  $\beta^* \approx 2500$  m. Both data sets allow the measurement of the elastic and total cross sections. In addition, the ultra-high  $\beta^*$  value gives access to the Coulomb region at very small values of the proton momentum transfer. This opens the possibility to measure the luminosity solely based on elastic scattering.

## Acknowledgments

We are indebted to CERN for the contributions to the construction and installation of the ALFA detector and its infrastructure. We acknowledge the help of all technicians and engineers in the collaborating institutions without whom the ALFA detector could not have been built. Explicitly we thank for the invaluable contributions during the design, construction, installation and commissioning phases of the Roman Pot stations: C. Cheikali, J.-L. Socha, D. Cuisy, C. Sylvia, B. Lavigne, M. Gaspard from LAL Orsay; C. David, J.-M. Lacroix, J. Noel, B. Salvant, M.v. Stenis from CERN; P. Pohl from DESY; T. König, M. Szauter from the JLU Giessen and M. Daniels, M. Jablonski from the HU Berlin.

Furthermore we are grateful to all the funding agencies which supported generously the construction and the commissioning of the ALFA detector and also provided the computing infrastructure. We acknowledge the supports from FCT Portugal grant CERN/FIS-NUC/0005/2015 and from Polish National Science Centre grant UMO-2015/18/M/ST2/00098.

## References

- [1] ATLAS collaboration, *The ATLAS Experiment at the CERN Large Hadron Collider*, [2008 JINST 3 S08003](#).
- [2] ATLAS collaboration, *ATLAS Forward Detectors for Measurement of Elastic Scattering and Luminosity*, [ATLAS-TDR-18](#) (2008) [CERN-LHCC-2008-004].
- [3] P. Grafström and W. Kozanecki, *Luminosity determination at proton colliders*, [Prog. Part. Nucl. Phys. 81](#) (2015) 97.
- [4] J.R. Cudell et al., *Hadronic scattering amplitudes: Medium-energy constraints on asymptotic behavior*, [Phys. Rev. D 65](#) (2002) 074024 [[hep-ph/0107219](#)].
- [5] COMPETE collaboration, J.R. Cudell et al., *Benchmarks for the forward observables at RHIC, the Tevatron Run II and the LHC*, [Phys. Rev. Lett. 89](#) (2002) 201801 [[hep-ph/0206172](#)].
- [6] U. Amaldi et al., *Measurements of the proton proton total cross-sections by means of Coulomb scattering at the CERN intersecting storage rings*, [Phys. Lett. B 43](#) (1973) 231.
- [7] P. Barrillon et al., *MAROC: Multi-Anode ReadOut Chip for MAPMTs*, in proceedings of the *IEEE-2006 Nuclear Science Symposium*, San Diego, U.S.A., October 29–November 2 2006.
- [8] P. Moreira et al., *A radiation tolerant gigabit serializer for LHC data transmission*, in proceedings of the *7th Workshop on Electronics for LHC Experiments*, Stockholm, Sweden, September 10–14 2001.

- [9] B. Hallgren and H. Burckhart, *Front-end I/O via CANBus of the ATLAS detector control system*, in proceedings of the *4th Workshop on Electronics for LHC Experiments*, Rome, Italy, September 21–25 1998.
- [10] S. Ask et al., *Luminosity measurement at ATLAS: Development, construction and test of scintillating fibre prototype detectors*, *Nucl. Instrum. Meth. A* **568** (2006) 588 [[physics/0605127](#)].
- [11] *EUDET: Detector R&D towards the International Linear Collider*, <https://www.eudet.org>.
- [12] S. Jakobsen, *Commissioning of the Absolute Luminosity For ATLAS detector at the LHC*, [CERN-THESIS-2013-230](#) (2013).
- [13] S. Franz and P. Barrillon, *ATLAS ALFA-measuring absolute luminosity with scintillating fibres*, *Nucl. Instrum. Meth. A* **610** (2009) 35.
- [14] A. Barriuso Poy et al., *The detector control system of the ATLAS experiment*, [2008 JINST 3 P05006](#).
- [15] A. dos Anjos, *The DAQ/HLT system of the ATLAS experiment*, [PoS\(ACAT08\)044](#) and online at <http://acat2008.cern.ch/>.
- [16] H. Boterenbrood et al., *The read-out driver for the ATLAS MDT muon precision chambers*, *IEEE Trans. Nucl. Sci.* **53** (2006) 741.
- [17] ATLAS collaboration, *Measurement of the total cross section from elastic scattering in pp collisions at  $\sqrt{s} = 7$  TeV with the ATLAS detector*, *Nucl. Phys. B* **889** (2014) 486 [[arXiv:1408.5778](#)].
- [18] ATLAS collaboration, *Measurement of the total cross section from elastic scattering in pp collisions at  $\sqrt{s} = 8$  TeV with the ATLAS detector*, *Phys. Lett. B* **761** (2016) 158 [[arXiv:1607.06605](#)] [[CERN-EP-2016-158](#)].